NOVA SCHOOL OF SCIENCE & TECHNOLOGY

DEPARTAMENTO DE CIÊNCIAS DOS MATERIAIS

Margarida Matias Neto da Silva Ribeiro

Licenciatura em Engenharia de Micro e Nanotecnologias

TEMPERATURE MONITORING FOR LITHIUM-SULFUR BATTERIES

MESTRADO EM ENGENHARIA DE MICRO E NANOTECNOLOGIAS

Universidade NOVA de Lisboa

Setembro, 2021

TEMPERATURE MONITORING FOR LITHIUM-SULFUR BATTERIES

MARGARIDA MATIAS NETO DA SILVA RIBEIRO
Licenciada em Engenharia de Micro e Nanotecnologias

Orientador: Doutor Luís Miguel Nunes Pereira, Professor Associado do Departamento de Ciência dos Materiais, Faculdade de Ciências e Tecnologia da Universidade Nova de Lisboa

Coorientadores: Doutor João Carlos da Palma Goes, Professor Associado com Agregação, Faculdade de Ciências e Tecnologia, Universidade Nova de Lisboa

Júri:

Presidente: Doutor Rodrigo Ferrão de Paiva Martins, Professor Catedrático do Departamento de Ciência dos Materiais da NOVA School of Science and Technology | FCT NOVA.

Arguentes: Doutora Joana Maria Dória Vaz Pinto Morais Sarmento, Professora Auxiliar Convidada, do Departamento de Ciência dos Materiais da NOVA School of Science and Technology | FCT NOVA;

MESTRADO EM ENGENHARIA DE MICRO E NANOTECNOLOGIAS

Universidade NOVA de Lisboa
Setembro, 2021

TEMPERATURE MONITORING FOR LITHIUM-SULFUR BATTERIES

Acknowledgments

Um agradecimento a todos que de alguma forma fizeram com que estes 5 anos fossem uma experiência única.

O meu agradecimento ao Prof. Doutor Rodrigo Martins e à Prof.ª Doutora Elvira Fortunato pela fundação do curso de Engenharia de Micro e Nanotecnologias, e pelas pelas condições oferecidas aos seus alunos através dos centros de investigação CENIMAT|i3N e CEMOP.

Ao meu orientador, Professor Luís Pereira por me ter ajudado e guiado ao longo desta tese. Obrigado também Professora Diana Gaspar, por toda a disponibilidade para me ajudar ao longo desta tese, sem si teria sido muito mais difícil ter alcançado estes resultados. Ao Professor João Goes por me ter emprestado a chave do laboratório de eletrónica, o que facilitou imenso e trabalho, e me permitiu ter as ferramentas necessárias para efetuar este trabalho. Ao Professor João Canejo por me ter facultado o leitor de disquetes, que se tornou imprescindível. A todas as pessoas do CENIMAT e do CEMOP que tiraram um pouco do seu tempo para me ajudar, muito obrigado.

Obrigado por todas as amizades que ganhei, Nia, Esteves, Raquel, Ricardo,Kika, Mariana Cortinhal, João Barroso, Filipe, Luís, Rui Guilhoto, Madeira, Eduardo, André, Célia, Margarida e muitos mais. À Annalisa pela amizade e por se ter tornado não só na minha companheira de casa como, mais importante, na minha companheira de jantares na PZA. À Lylia, pelas caminhadas por Sintra e as tardes passadas na esplanada da praia a falar sem pausas. Ao Pedro um especial obrigado, por me ensinar muitas coisas ao longo destes anos, e me fazer crescer. À Beatriz, pela amizade desde a catequese, e por tantos momentos bons passados, apesar de vivermos em margens opostas.

Um agradecimento a toda a família, aos tios, aos primos (Zé e Fati), Tio João, Tio Rui, Kimberley, Belinha, aos Nunos e Sofia. À minha madrinha, ao tio César e ao Tomazinho por sempre me apoiarem. Um agradecimento especial à Tina, ao Francisco e à Maria por me fazerem sentir em casa sempre que os visitei.

E por fim, o maior agradecimento é para a minha mãe, (mãe és a melhor), que me apoio e ajudou sempre, se não fosse ela nada disto seria possível.

Resumo

Com a crescente modernização do mundo em que vivemos, a evolução das baterias é um dos requisitos mais importantes. As baterias Li-S têm potencial para responder às necessidades do mercado, mas para além da sua capacidade de armazenamento de energia, a sua segurança também é imprescindível. Ter um sistema que nos permite monitorizar o que se passa no interior da bateria, nomeadamente no interior do electrólito, é extremamente vital para garantir essa segurança.

Os sensores fabricados e estudados neste trabalho podem ser o primeiro passo em direção a um sistema para verificar em tempo real como as mudanças ocorrem dentro de uma bateria.

Neste trabalho é feita a fabricação dos sensores compostos por titânio e cobre e o mecanismo utilizado para estudar o sensor é o seguinte:

O sensor é conectado a um analisador vetorial que fará uma varrimento da frequência. Quando a frequência do sinal está próxima da frequência natural do sensor, o sensor ressoa. Extraindo o ponto mais baixo da curva de frequência vs. S_{11}, a frequência de ressonância do sensor pode ser obtida.

Para este sensor foram identificados três picos distintos, associados à frequência de ressonância. O pico entre 0.93 e 1.16 GHz foi o que demonstrou ser mais promissor para ser usado na medição da temperatura, devido a ter uma maior sensibilidade em comparação com os outros dois.

Os resultados mostraram que ao aumentar a temperatura, a frequência de ressonância do sensor diminui. Embora para medições do sensor incorporado com o eletrólito, a resposta não foi tão linear quanto o esperado, o que pode ser devido a fatores como o tipo de solvente usado para o eletrólito, humidade e a possível degradação dos polímeros usados no eletrólito.

Palavras-chave: Sensor, Eletrólito polimérico, Frequência de ressonância, Bateria de lítio-enxofre, Monitorização da temperatura interna, circuito RLC.

Abstract

With the increasing modernization of the world in which we live, the evolution of batteries is one of the most important requirements. Li-S batteries can meet the demands of the market, but in addition to their energy storage capacity, their safety is also imperative. Having a passive system that allows us to monitor what is going on inside the battery, namely inside the electrolyte, is extremely vital to ensure the safety of the battery.

The sensors manufactured and studied in this work can be the first step towards a system to check in real-time how changes are happening inside a battery. In this work, the fabrication of the sensors composed of titanium and copper is made and the mechanism used to study the sensor is as follows:
The sensor is connected to a network analyzer that will make a frequency sweep. When the frequency of the sweep signal is close to the natural frequency of the sensor, the sensor resonates. By extracting the lowest point of the frequency vs. S_{11} curve, the resonant frequency of the sensor can be obtained.

For this sensor, three distinct peaks were identified, associated with the resonant frequency. The peak between 0.93 and 1.16 GHz was the one that proved to be the most promising to be used in temperature measurement, due to its greater sensitivity compared to the other two.

The results showed that when increasing temperature, the resonance frequency of the sensor decreases. Although for measurements of the sensor incorporated with the electrolyte, the response was not as linear as expected, which could be due to factors such as the type of solvent used for the electrolyte, humidity, and the possible degradation of the polymers used in the electrolyte.

Keywords: Sensor, Polymer electrolyte, Resonance frequency, Lithium-sulfur battery, RLC, Internal temperature monitoring.

Acronyms

DSC – differential scanning calorimetry

Li-ion – Lithium-ion

LiPS – Lithium polysulfides

Li-S – Lithium-sulfur

PAN – Polyacrylonitrile

PEO – Poly (ethylene oxide)

PMMA – Poly (methyl methacrylate)

PVdF –Polyvinylidene fluoride

STA – Simultaneous thermal analysis

TGA – Thermogravimetric analysis

THF – Tetrahydrofuran

List of Symbols

C – Capacitance

D - Diameter

d – Distance between electrodes

$\boldsymbol{\varepsilon_0}$ **-** Permittivity of vacuum

$\boldsymbol{\varepsilon_r}$ – Relative permittivity

R - Resistance

S – Area of facing electrodes

$\mathbf{S_{11}}$ – Reflection coefficient

$\mathbf{T_g}$ – glass transition temperature

$\mathbf{Z_0}$ **-** Characteristic impedance of the system

$\mathbf{Z_R}$ **-** Equivalent complex impedance

Table of Contents

List of figures

List of tables

1 Introduction

The increasing demand for electric storage systems in the fields of portable electronic devices and electric vehicles brings urgency to the development of new rechargeable batteries with higher energy density to substitute the commercial lithium-ion (Li-ion) batteries currently used.[1] The lithium-sulfur (Li-S) battery is one of the most promising alternatives to the Li-ion and is receiving rapidly growing research interests due to the extremely high energy density and abundant resources of sulfur.[2]

This section starts with a brief overview of the working principle of Li-S batteries, including the problems that may be delaying the implementation of this technology in the market. These problems can have consequences related to the safety of the battery, and the substitution of liquid electrolytes by polymer ones can be an option to improve the safety and performance of the Li-S batteries. This introduction intends to give the reader the required basic battery knowledge and to highlight the importance of measuring internal battery temperature to have safer batteries. After that, different available temperature measurement methods for batteries are presented, and it is introduced the approach to measuring temperature that will be discussed in this thesis.

1.1 Lithium-sulfur battery

Sulfur (S), one of the materials that have been receiving wide attention for energy storage applications, is an important element of the Li-S battery. It is a yellow solid nonmetal, a cyclic molecule (S_8) consisting of eight atoms. Elemental sulfur is abundant and has been an actively researched cathode material in the last decade.[3] The use of sulfur as a cathode material has become very attractive for next-generation energy storage devices due to being a low-cost material with high energy density, and non-toxicity. One of the most promising characteristics of a sulfur-based cathode is its high theoretical specific capacity of 1675 $mAh.g^{-1}$ and an energy density of 2600 $Wh.kg^{-1}$, which is three times higher than conventional cathodes.[4]

1.1.1 Components and operating principles

The Li-S battery is an energy storage device that converts the chemical energy of lithium and sulfur, to electrical energy through electrochemical reactions. In a Li-S cell, the positive electrode consists of a porous, electronically conducting host, a vital component that delivers electrons to the insulating sulfur. Upon discharge, lithium ions move spontaneously through the electrolyte from the negative electrode while electrons flow through the external circuit, delivering electrical energy, as shown in figure 1.[5]–[7]

The discharge process of the battery occurs with a sequence reaction of sulfur, which first produces soluble polysulfides and then insoluble polysulfides. The chemical reactions in the charging process include the reversed reactions of those in the discharge process.

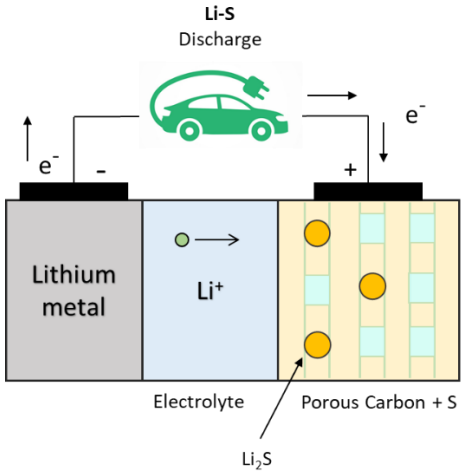

Figure 1 - Schematic of the working principle of the discharge of a Li-S battery. This example illustrates a battery that is composed of a negative electrode (lithium metal), a positive electrode (sulfur in a porous carbon matrix), and an electrolyte. The blue squares symbolize the porous character of the carbon. Adapted from [1]

1.1.2 Limitations of Li-S batteries

Besides numerous promising features of sulfur as cathode active material, few inherent challenges still obstruct the widespread commercialization of the Li-S battery system. Difficulties in their practical application are related to the nature of the electronic and ionic conduction of sulfur and its discharge products. The dissolution of the lithium polysulfides (LiPS) leads to the shuttle effect, significant loss of active cathode material, and lithium corrosion on the anode (figure 2). [4] In Annex 1 it can be found a more extensive explanation of the difficulties that the Li-S batteries are facing.

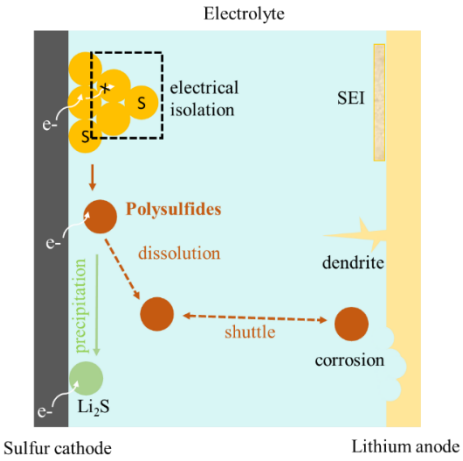

Figure 2 – Schematic illustration of the limitations of Li-S batteries. Adapted from [8].

1.1.2.1 Safety hazard

The implementation of Li–S batteries is still slow due to the main challenges that were referred to previously, such as low electrical conductivity of sulfur and its discharge products, large volumetric change during charging/discharging, the high solubility of LiPS species, and the related shuttle effect.

Over the past decade, considerable efforts and strategies have been explored to improve the performance of the Li–S battery. Tremendous progress has been achieved in the laboratory with high energy density and excellent cycling stability.[9] Even so, there is still a long way to go before applying the Li–S batteries to electric vehicles and portable electronic devices in our lives, with the main public concerns on the safety

hazards. The underlying safety hazards of Li-S batteries mainly arise from the reaction of highly active polysulfides with metallic lithium especially at high temperatures, causing the formation of dead lithium and corrosion of the anode. [10]

1.1.2.2 Polymer electrolytes

Conventionally used organic liquid electrolytes in Li-S batteries with a low flash point (2ºC) are a serious concern in terms of safety. Liquid electrolytes containing lithium salts such as lithium perchlorate ($LiCl_4$) and lithium trifluoromethanesulfonate ($LiCF_3SO_3$), and a mixture of ethers (linear or cyclic) as tetrahydrofuran (THF) and dimethoxyethane are the traditional choice in most lithium batteries.[11] Flammable and volatile electrolytes, such as 1,3-dioxolane/1,2-dimethoxyethane (DOL/DME), are susceptible to ignition due to the possibility of thermal runaway during cell cycling. [12][13]

Recent developments in electrolyte systems for Li–S batteries, especially in polymer electrolytes are being made. They have the potential to combine the advantages of high ionic conductivity and good mechanical properties that can physically block polysulfide diffusion. Polymer electrolytes generally have an ionic conductivity in the range from 10^{-8} to 10^{-4} $S.cm^{-1}$. They can be used in a variety of applications and are found in thin-film batteries, electrochromic displays, fuel cells, and supercapacitors.[14]

Swapping liquid electrolytes for polymer electrolytes has the potential to make the battery intrinsically safer, in terms of preventing leakage of a potentially dangerous liquid. Concerning the operation of the lithium-sulfur system, some form of polymer electrolyte may directly improve, or prevent, the processes that appear to be inevitable in the liquid electrolyte systems investigated to date. [15]

So far, polymer hosts as poly (ethylene oxide) (PEO), polyacrylonitrile (PAN), polyvinylidene fluoride (PVdF), and poly (methyl methacrylate) (PMMA) have been developed and characterized. Their characteristics are explained in detail in Annex 2.

1.1.2.3 Thermal issues in Li-S batteries

It is urgently necessary to fabricate a highly stable and safe lithium-sulfur battery that fundamentally avoids thermal issues under various abuse conditions, such as short-circuit, overcharging, or impact. Moreover. battery thermal management of the energy storage system is critical to its performance and safety, especially for Li-S batteries with high density.[16] The batteries with higher energy density may have lower thermal stability, leading to safety hazards, such as thermal runaway.

Thermal runaway in Li-S batteries

Thermal runaway (TR) is known to be the most catastrophic failure mode of batteries, with scarce research being done on the evaluation of the thermal runaway features of Li–S batteries until now. The safety issues have become a bottleneck in the commercialization of Li–S batteries and make the high energy density Li–S batteries followed by an uncertain future, of which the development may stagnate for many years. Thus, the safety issues of Li–S batteries, particularly associated with thermal runaway behaviors, require in-depth investigation.[17]–[20]

TR occurs when parts of the cell exceed a critical temperature and initiate exothermic reactions. The initial undesired temperature rise might be caused by electrical or mechanical abuse, or as a result of an external heat source.[16] Is well known that mechanical abuse and over-heating can trigger the Li–S batteries to thermal runaway with smoke, fire, and even explosion, which attracts public concerns about the safety problems. Furthermore, in battery packs where the cells are connected in parallel and/or in series, once one cell undergoes TR, the released heat may cause the whole module to get into thermal runaway.[21]. The failure mechanism is closely associated with safety and needs to be fully understood.[22] To predict the occurrence of TR and

then prevent Li–S batteries from TR, Huang et al. [23] conducted a study that evaluated the TR features of a Li–S cell at various states of charge and suggested that the major heat source during TR may not be the internal short circuit but the redox reaction between cathode and anode.

1.2 Review of the state-of-the-art temperature monitoring for batteries

The focus of the next paragraphs will be the review of the devices and methods used to monitor the internal temperature in batteries. The literature described in this section is limited to temperature measurement methods and sensors for Li-ion batteries since there are no reports of these methods and sensors used in Li-S batteries. Considering the similarities between the two types of batteries, we may infer that these same methods and sensors could be used in Li-S batteries as well.

The first and utmost challenge in designing a battery system is to ensure its inherent safety under both normal and abuse operating conditions. To this goal, knowledge of thermal behavior is critical. Different approaches are being made to monitor the changes that occur on a battery. As in any other electrochemical energy storage system, the chemistry of the active materials alters during the charge/discharge processes, promoting strains in electrode particles and changes in electrode volume. [24]

The distribution of temperature at the surface of batteries is easy to acquire with common temperature measurement approaches, such as the use of thermocouples and thermal imaging systems. Most past papers have only measured cell temperature on the outer surface and not the core temperature. [25][26] Internal monitoring is problematic due to the chemically aggressive and electrically noisy environment, for which sensors with low invasiveness, mechanical robustness, and corrosion resistance are required. The self-production of heat during operation can elevate the temperature of the battery from the inside. The transfer of heat from the interior to the exterior of the battery is difficult due to the multi-layered structures and low coefficients of thermal conductivity of the battery components, and the distribution of internal temperature is also uneven. In consideration of the sealed nature and the electrochemical reactions of batteries during operation, researchers tried to explore different approaches in monitoring the internal temperature of batteries. A limited number of techniques that have been evaluated for measuring the internal temperature of the cell can be divided into two main categories, contact measurement, and contactless measurement. [27]–[29]

In contact measurement, temperature sensors such as thermocouples and fiber Bragg grating sensors are inserted into the battery to measure the temperature directly. In contrast, in the contactless measurement, the internal temperature is obtained indirectly without intruding into the batteries. Modeling simulation and electrochemical impedance are two major contactless approaches. In the modeling simulation, electrochemical and thermal models were established to simulate the operation of the battery in different situations and theoretically estimate the internal temperature.[30]–[32] Annex 3 will feature an overview of the present approaches for both contact measurement and contactless measurement of the internal temperature of the Li-ion batteries.

1.3 LC sensor

The LC sensor (Figure 3a) is used to monitor a wide range of parameters, such as biochemical, gas, humidity, temperature, strain, and pressure. This device senses when the parameter of interest changes, subsequently resulting in a shift in its resonance frequency. To wirelessly obtain data from the LC sensor, a readout coil is magnetically coupled with the sensor, and the resonant frequency of the sensor is detected through monitoring the input return loss (Figure 3b) of the readout coil. [33][34]

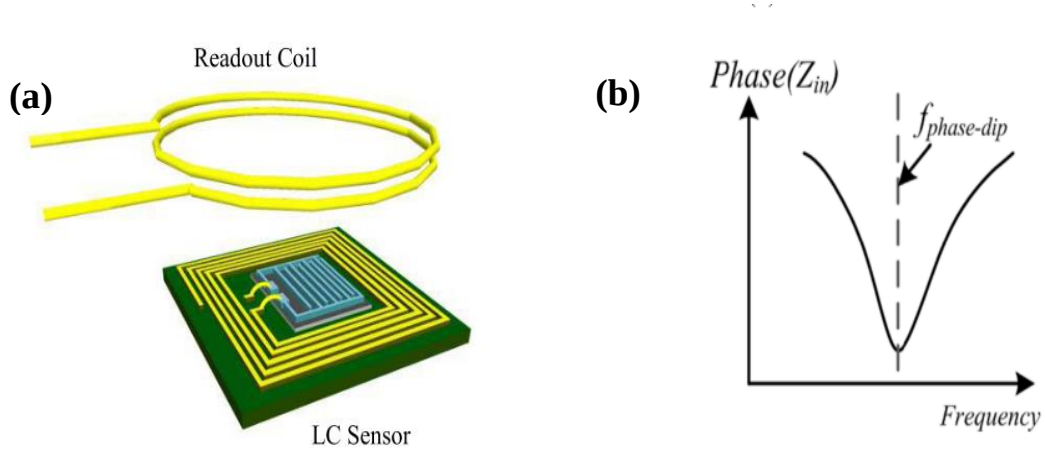

Figure 3 – **(a)** Schematic representation of an LC sensor and its interrogating system. **(b)** The characteristic curve of Phase (Z_{in}) Adapted from [33]

In most cases, the LC sensors are printed or deposited on the surface of a component to form a planar structure composed of an inductor (L) and an interdigitated capacitor (C) connected in series. The main principle of the LC temperature sensor is based on the change in capacitance concerning the temperature. The change in capacitance will alter the resonant frequency, as shown by equation 1, and that resonant frequency is unique to every temperature. The shifts in the resonant frequency can be wirelessly detected and temperature data can be inferred. The inductor which is connected in series to complete the LC sensor circuit is used to absorb and re-radiate the electromagnetic radiation which enables wireless interrogation capability of the sensor.[35][36]

$$f_0 = \frac{1}{2\pi\sqrt{LC}} \tag{1}$$

Wang et al. [37] proposed a study for multiresonance and passive inductance capacitance temperature and strain sensor. The results showed that the sensor fabricated on a polyimide film using electroplating technology, had stable operation between 25 ºC and 85 ºC with an average sensitivity of 27.3 kHz/ºC, as presented in figure 4a and 4b.

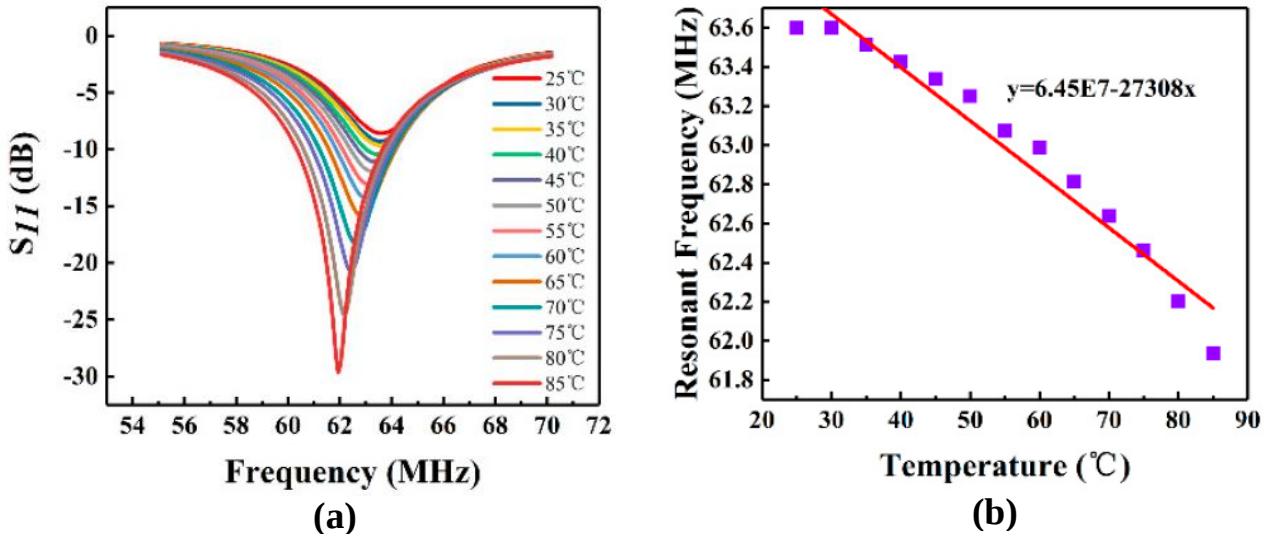

Figure 4 – **(a)** View of the temperature response curve of the sensor between 25 ºC and 85 ºC. **(b)** fitted curve of the temperature response curve. [37]

1.3.1 RLC Sensor

Our approach is that instead of an LC sensor, a sensor with an RLC (Resistance-Inductor-Capacitor) equivalent circuit will be designed and fabricated. The sensor will have its resonance frequency peaks which will be studied to investigate how they change with the temperature. The goal is for this sensor to be incorporated inside the battery, and that with the temperature variation it is possible to observe a shift in the peaks of the resonance frequency of the sensor.

Below are listed key requirements that were identified for this sensor to have minimally intrusive sensing inside the Li-S battery:

1. The sensor cannot react with or dissolve in the battery electrolyte.
2. Transport or transfer of ions between electrodes cannot be affected due to the presence of the sensor.
3. The sensor must be compatible with the cell assembly process.

This thesis will focus on the sensor behavior with temperature variation, and also assess how it behaves in contact with the electrolyte (hence the reason for casting electrolyte on top of the sensor).

This sensor will work as an RLC circuit, it has a resistance (R), a capacitance (C) that will exist between the lines, and an inductance (L). The equivalent circuit of the sensor is shown in figure 5.

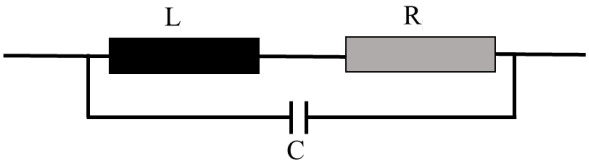

Figure 5 - Equivalent circuit of the sensor.

Just as the resonance formula exists for LC circuits (equation 1), for the equivalent sensor circuit manufactured, the resonance frequency equation (equation 2) depends not only on L and C but also on R.

$$f_0 = \sqrt{\frac{1}{LC} - \left(\frac{R}{L}\right)^2} \tag{2}$$

2

Materials and Methods

2.1 Sensor fabrication

The sensors were fabricated on a glass subtract of 2.5 × 2.5 cm. The sensor production is graphically explained in Figure 6, where it is possible to see what materials were used and what is their function in this process.

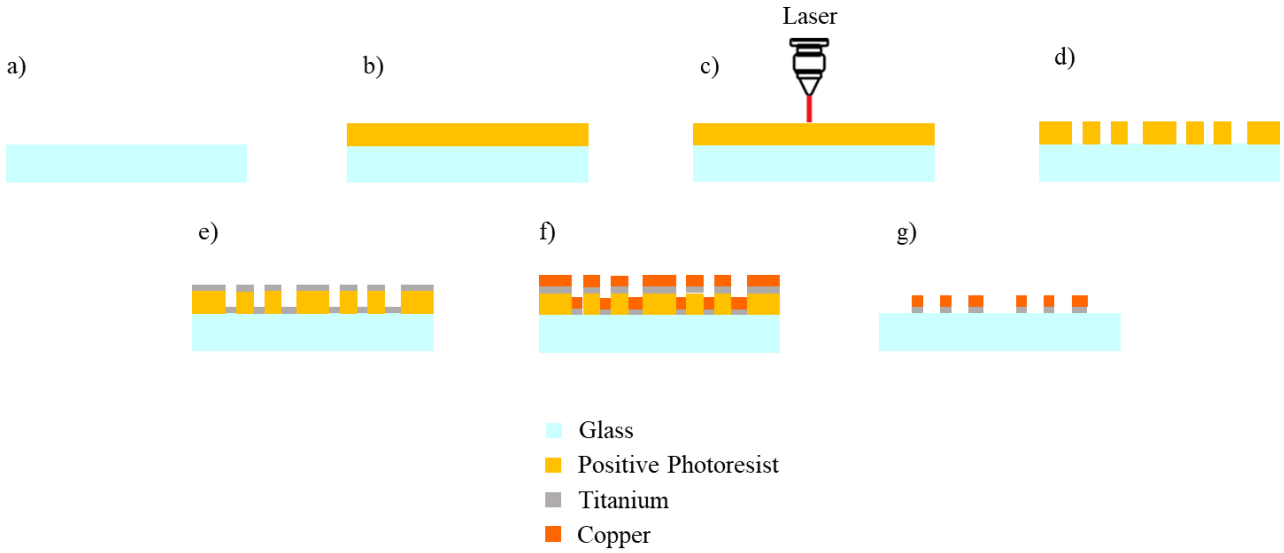

Figure 6 – Schematic of the sensor fabrication steps. Cross-section view.

The fabrication followed these steps:

Step a) Substrate cleaning: An acetone bath, isopropyl alcohol (IPA) bath, and water bath, in ultrasounds for fifteen minutes each to prepare the substrate for the deposition.

Step b) A layer of positive photoresist (AZ ECI 3007) is spread on the substrate. Annealing of 1 minute and 30 seconds was made.

Step c) With the Heidelberg µPG 101 Tabletop Micro Pattern Generator, and a write head of 20 mm, the laser draws the sensor previously designed on software (*KLayout*).

Step d) The photoresist is developed (AZ 726 MIF) and the zone that was exposed by the laser is now free of photoresist.

Step e) The deposition of a 20 nm layer of titanium by E-beam assisted physical vapor deposition.

Step f) The deposition of a 200 nm layer of copper also by E-beam assisted physical vapor deposition (the deposition parameters for both titanium and copper are represented in Table 8 – Annex 2).

Step g) The final step is the lift-off, where the samples are put on acetone until all the photoresist and excess of material deposited previously is no longer on the substrate, only the material that was having direct contact with the substrate stays.

2.2 Network analyzer

For the analysis of the resonance frequency of the sensors, the Agilent Technologies 8753ES Option 011 network analyzer was used. Only port 1 was utilized and calibrated before every measurement between frequencies from 30kHz to 6 GHz. The sensor is weld to an SMA (SubMiniature version A) connector with two copper wires, one must be linked to the ground (center of the SMA connector) and the other to one of the remaining accesses. Finally, the connector is coupled to a line in Port 1 of the network analyzer as shown in figure 6.

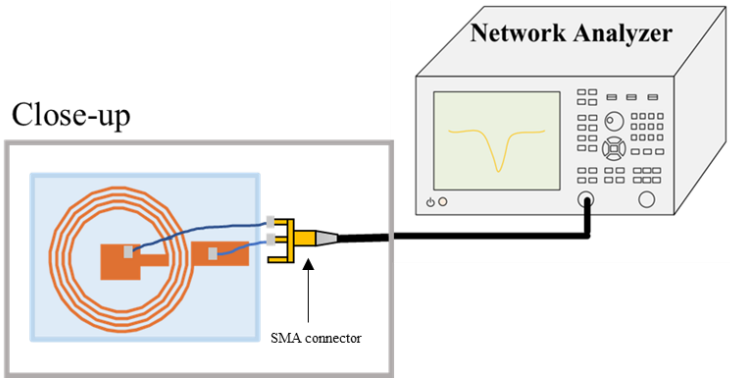

Figure 7 - Setup for the sensor analysis.

2.3 Electrolyte

For the electrolyte synthesis, the following reagents were used as received, without further purification: PMMA (Poly (methyl methacrylate)) from Diakon, EC (ethylene carbonate) from Fluka with 99% purity, $LiCF_3SO_3$ (lithiumtrifluormethansulfonat) from Sigma-Aldrich, and THF (tetrahydrofuran) from Sigma-Aldrich. The production method followed was described elsewhere by Sun et al. [38]. A mixture of 0.9188g of PMMA, 0.3056g of EC, and 0.4083g of lithium salt is weighted and put on a glass recipient. The mixture is dissolved in 8 mL of THF and stirred continuously (600 rpm) at room temperature until a homogenous and transparent solution is obtained. The solution is then poured into the top of the sensor that lays on aluminum foil and left for 24 hours to allow the excess solvent to evaporate off slowly, at room temperature until thin films are formed. The produced film was also trimmed into samples for characterization of Simultaneous Thermal analysis (STA). To have the same amount of electrolyte in every sample, 5 mL of it were cast on top of the sensor and were left to dry.

2.3.1 Simultaneous Thermal analysis

During this work, the STA was used as a complementary technique to infer the thermal stability of the electrolyte. The STA refers to the simultaneous thermogravimetric analysis (TGA) and differential scanning calorimetric (DSC) measurements of a sample in the same instrument. A heating rate of 5 °C/min was used from 25 to 350 °C when acquiring information from the Netzsch 449 F3 Jupiter® simultaneous thermal analyzer.

3 Results and Discussion

This section will be focused on the manufacture of the sensors, where the design and fabrication of the titanium/copper sensor on a glass substrate will be displayed. Also, with the network analyzer, the resonance frequencies of the sensor will be obtained, and the results acquired will be discussed.

3.1 Sensor design and fabrication

3.1.1 Design

One of the objectives of this work was the production of the sensors. The design used is shown in Figure 8. The choice of the sensor size and design did not target a specific requirement, but it was desirable that the sensor should have a peak between 30 MHz and 6 GHz, so that it could be analyzed by the network analyzer.

The design was made using the software KLayout. The two large blocks (one inside and the other outside) were made so that it was easier to later weld the wires to connect to the network analyzer. The width of the lines is 350 µm and the space between them is 450 µm, as shown in Figure 9.

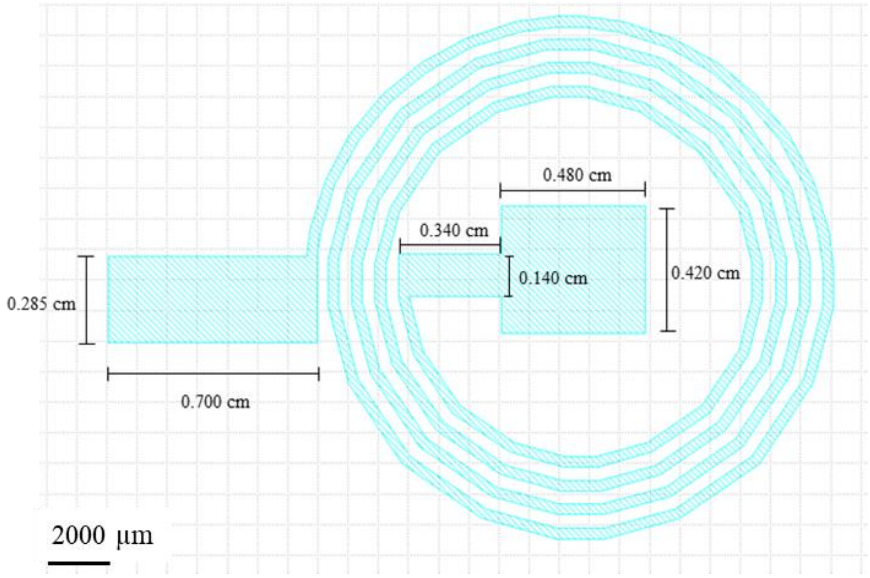

Figure 8 - Design of the antenna with the KLayout program.

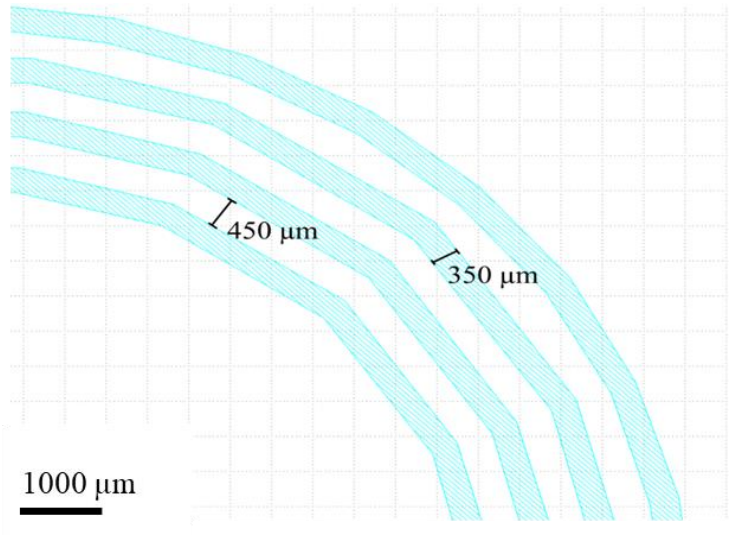

Figure 9 - Detail of the lines of the antenna.

To confirm that the sensor fabricated was according to the design, photographs of both the sensor (figure 9a) and the detail of the lines (figure 9b) were taken. These images were taken by the Optical Stereo Microscope - Leica M80, where the length of the lines and the space between them are exhibit.

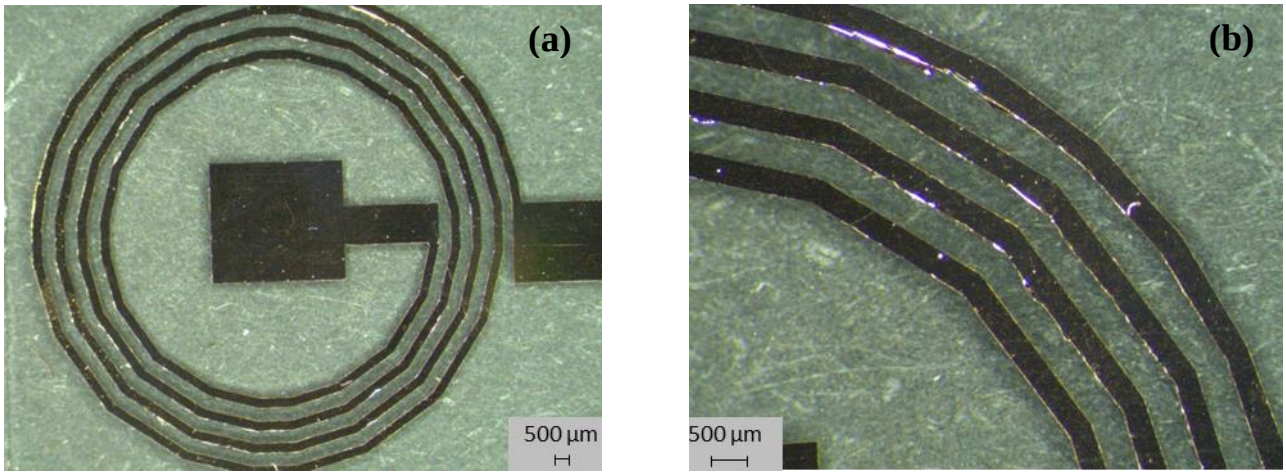

Figure 10 – **(a)** Optical microscope photograph of the antenna obtained after the process. **(b)** Optical microscope photograph of the detail of the antenna was obtained after the process.

In this case, the sensor design was inspired by an antenna. For antennas whose geometry is circular, the variable *A* (equation 2) is first determined, to later determine the inductance value (equation 3):

$$A = \frac{D + N(w + s)}{2} \tag{2}$$

$$L = \frac{A^2 N^2}{30A - 11D} \tag{3}$$

where *D* corresponds to the value of the internal diameter, *w* to the width of the turns, and *s* to the spacing between tracks, all expressed in inches, *N* to the total number of turns, and *L* corresponds to the value of the inductance in µH. The values of the design parameters are displayed in table 1.

Table 1 - Design parameters of the sensor.

Parameters	Values
D [in]	0.477
N	4
w [in]	0.014
s [in]	0.017
A	0.299
Thickness	442.5 µm

The values for the resistance of the sensor are presented in Table 4 (annex 3). The resistance of the sensor samples varies between 23.1 Ω and 32.7 Ω. Therefore, it is expected that the resonance peaks will be different between samples.

3.2 Resonance frequency

S-parameters such as S_{11} describe the input-output relationship between ports (or terminals) in an electrical system. For instance, if we have 2 ports (port 1 and port 2), then S_{12} represents the power transferred from port 2 to port 1. In this work, only S_{11}, also known as reflection coefficient, will be used since the sensor was only connected to port 1. Equation 5 displays how the network analyzer obtains S_{11}.

The mechanism used to study the sensor is as follows: The sensor is connected to a network analyzer that will make a frequency sweep. When the frequency of the sweep signal is close to the natural frequency of the sensor, the sensor resonates. By extracting the lowest point of the frequency vs. S_{11} curve, the resonant frequency of the sensor can be obtained. An example of a resonance peak is demonstrated in figure 11.

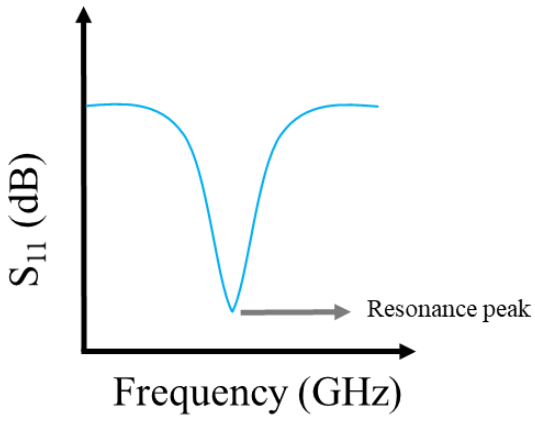

Figure 11 – Example of a frequency vs S_{11} curve.

$$Z_R = Z_0 \times \frac{1 + S_{11}}{1 - S_{11}} \quad (5)$$

Z_R - Equivalent complex impedance;

Z_0 - Characteristic impedance of the system;

S_{11} – Reflection coefficient.

As mentioned earlier in equation 4, the resonance frequency is dependent on three variables, the inductance, the capacitance, and the resistance of the sensor. It is expectable that if the frequency peaks change with temperature, one of them, or even all those variables could change. Due to equipment-related limitations, it was not possible to obtain graphs relating inductance/capacity/resistance to temperature, so the analysis of this work will be focused only on analyzing how the resonance peaks change.

With the network analyzer, peaks of the resonance frequencies of the sensors are obtained, to be able to analyze how those peaks behave with temperature variation. The accuracy of the network analysis is greatly influenced by factors external to the network analyzer. Components of the measurement setup, such as interconnecting cables and adapters, introduce variations in magnitude and phase that can mask the actual response of the device under test. To make this analysis more reliable, the acquisition of a calibration line is necessary before any measurements are made. After the calibration procedure, the graph showed in figure 12 was obtained. It can be noted that exists a resonance peak at 1.77GHz, so for our analysis of peaks, 1.77 GHz will not be considered as the resonance peak of the sensor.

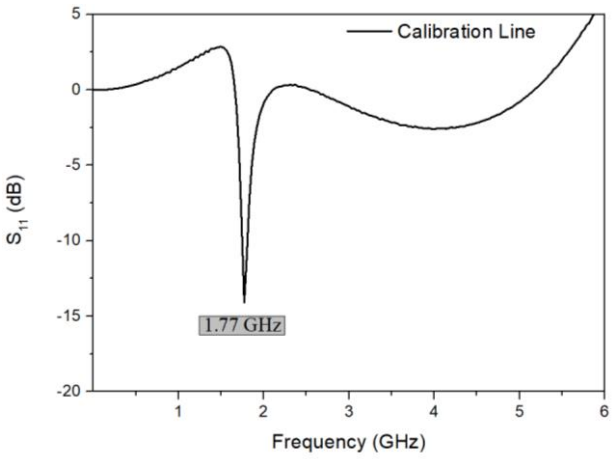

Figure 12 - Graph obtained after calibration from 30 MHz to 6 GHz. The number of sampling points of the network analyzer was set to a maximum of 201 points.

3.2.1 Resonance frequency at ambient temperature

The first analysis being made is to acquire the resonance peaks of the sensor at ambient temperature (T = 25ºC), in figure 13 is presented the sensor studied. After analyzing identical samples, the graph displayed in figure 14 was obtained. In order to make the analysis of the resonance peaks simpler, it was chosen to divide the graph into two zones. Zone A, which goes from 30 MHz to 2.5 GHz, and zone B, which goes from 2.5 GHz to 6 GHz. This decision was made since there is a bigger discrepancy between equal samples in zone B, while in zone A the peaks are relatively constant in terms of resonance peaks.

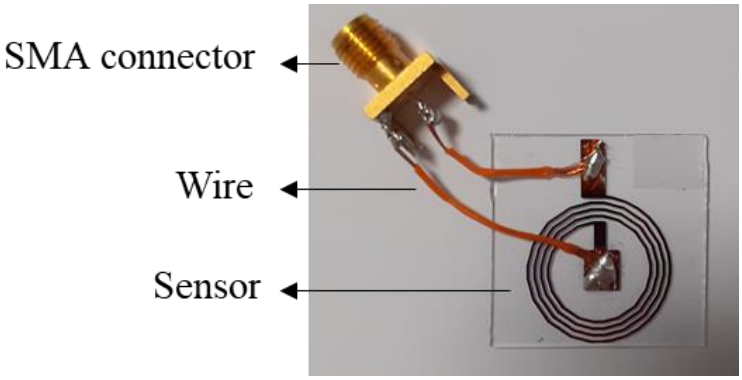

Figure 13 - Photograph of the sensor connected to the SMA connector.

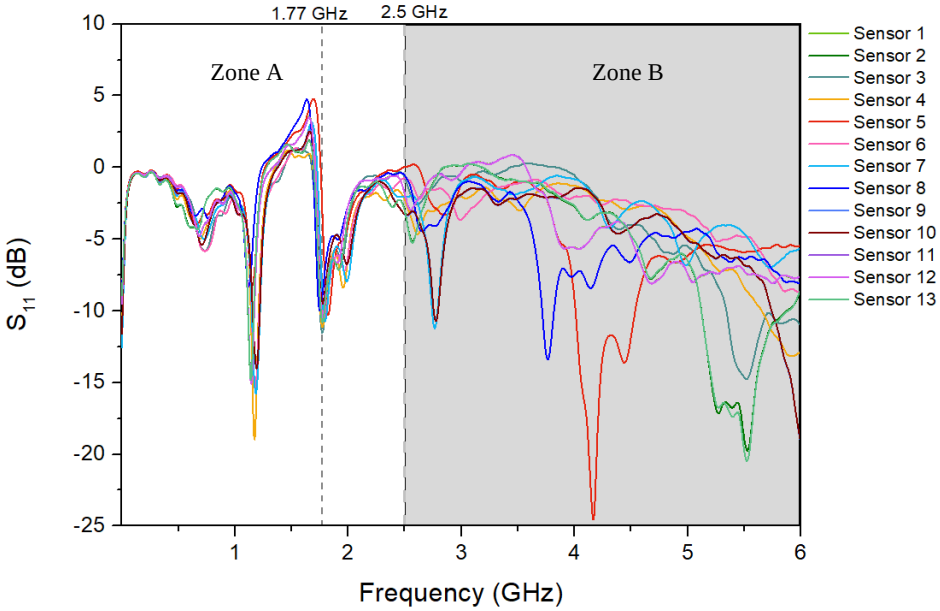

Figure 14 - Graph of the resonance peaks of all the samples.

This inconsistency between sensors on zone B could be related to the welding process or associated with the wires used to connect the sensor to the network analyzer. Throughout the next sections, the focus will be on peaks from zone A.

In zone A, it was identified three potential resonance peaks, as displayed in figure 15. The three potential peaks are signalized in grey areas and will be analyzed further. A closer look at zone A shows that the peak at 1.77 GHz previously referred to as associated with the equipment calibration and not with the sensor, in this graph appears to shift position. This change could be explained by the fact that there is a sensor resonance peak close to that frequency, which despite not showing up clearly in the graph, causes the peak that was previously at 1.77 GHz to now to appear slightly shifted to the sides.

As observed in the graph, the resonance peak 2 is the one with the greatest amplitude, which, based on the analysis method we are performing, means that it is the frequency at which the sensor has the greatest agreement with the system impedance, 50 Ω.

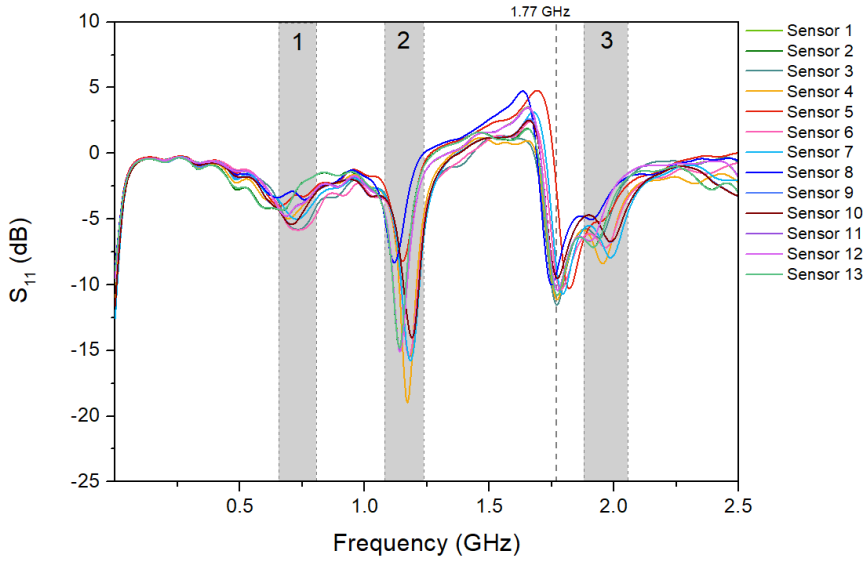

Figure 15 - Graph of the resonance peaks of all the samples [Zone A] The grey areas represent the resonance peaks that will be analyzed further.

In table 2, the three potential resonance peaks of the sensor that were signaled in grey in figure 15 are exhibit. As displayed, peak 2 is the one that has the least deviation from the three, which could facilitate the evaluation of changes with temperature, between identical samples. The deviation presented is the deviation from the average value.

Table 2 - Resonance peaks zone A at ambient temperature (all samples).

Peak Nº	Frequency [GHz]	Deviation
1	0.703	±0.03
2	1.15	±0.02
3	1.94	±0.03

To better understand the work in the next sections, it is important to clarify the range of frequencies that will be considered for each peak. This clarification is necessary because along with the results discussion the frequency associated with the peaks changes. For example, peak 1 will vary between 0.57 GHz and 0.70 GHz. The frequency range associated with each peak is displayed in table 3.

Table 3 - Frequency range associated with each peak.

Peak Nº	Frequency [GHz]
1	0.57 to 0.70
2	0.93 to 1.16
3	1.81 to 2.01

To find explanations for this variation between samples fabricated under the same conditions, a plot was made to compare the resistances of the samples, to understand if there was a linear relationship between the resonance peak 2 being more to the right or the left and the greater or smaller resistance of the sample. Peak 2 was chosen for this comparison due to being the one where the amplitude was bigger.

When looking at the graph in figure 16, it can be observed that there is no direct relationship between the sensor resistance and the resonant frequency of peak 2. This is not to say that there is no relationship, as there are a set of factors other than the resistance that influence the resonance frequency. Those factors could include the type of wire used for the welding or even the welding itself.

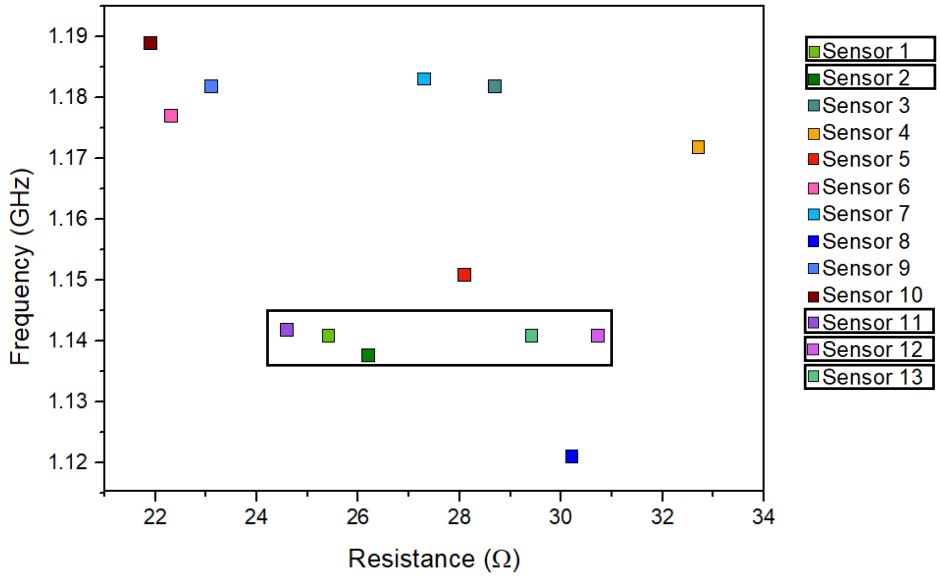

Figure 16 - Graph of the frequency of the second peak in relation to the resistance of the sensor. Surrounded by a black rectangular are the sensors that were used for the further analysis with temperature and electrolyte.

Although with different resistances, sensors 1, 2, 11, 12, and 13 present a very similar value for the three peaks. For that reason, and for the analysis to be as accurate as possible, those sensors were chosen to perform further analyses, due to having a similar S_{11} response for the three peaks, as shown in the graph of figure 17.

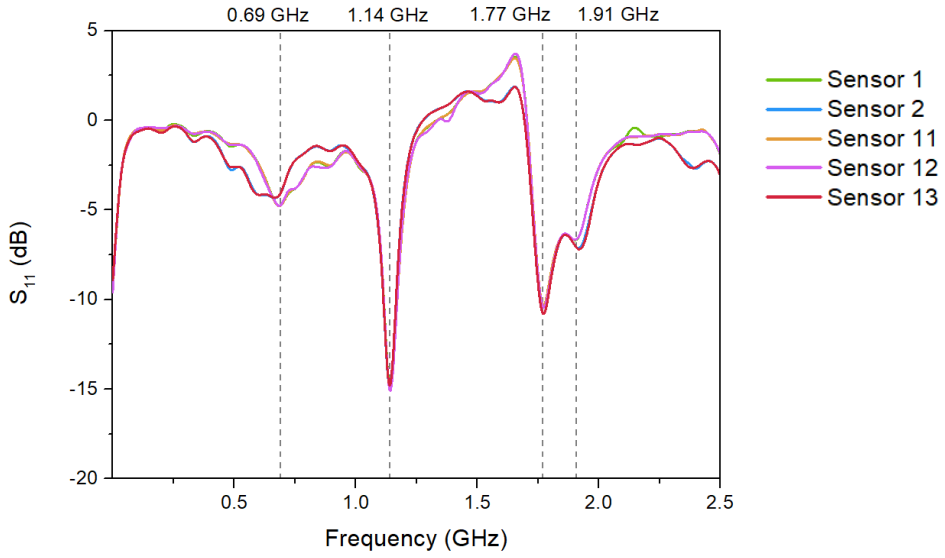

Figure 17 - Graph of sensors 1,2,11,12,13 without temperature variation. (Every sensor had a frequency sweep between 30 MHz and 2.5 MHz 30 times, to prove that the peaks did not suffer any change without variation of the temperature, T = 25 ºC). Although sensors 1, 2, and 11 are represented in the graph, since they have very similar graphics to sensors 12 and 13, they are superimposed.

The values of frequency of the three peaks are presented in table 4, but this time only sensors 1, 2, 11, 12, and 13 were counted. For all three peaks is noticeable that the deviation is smaller than previously, which was expected, especially for peak 2.

Table 4 - Resonance Peaks Zone A (sensors 1,2,11,12,13).

Peak Nº	Frequency [GHz]	Deviation
1	0.6862	±0.0131
2	1.141	±0.0009
3	1.909	±0.0076

The objective of this work is to investigate if the sensor fabricated could be used as a temperature sensor. As discussed before, the sensor has three resonance frequencies (three peaks). It is expected that at the end of this work results show what resonance frequency is ideal for sensing temperature.

To investigate how the sensor behaves at different temperatures, several analyses were carried out to better understand its behavior. The first is done by turning the heating plate on at 150ºC and recording data every 5 seconds. This analysis will provide a more general idea of how the resonance peaks change, and which peak(s) should be further analyzed. The second is done by recording the frequency values for the respective temperature values. In this case, steps of 10ºC were made, starting at 30ºC, and ending at 150ºC.

3.2.2 Resonance frequency with temperature variation

As previously explained, this first measurement was made to examine what peaks have a change in the resonant frequency with temperature. Observing the graph in figure 18a, which is demonstrating the behavior of the sensor being heated at 150ºC, the resonance peaks at 0.686 GHz, 1.14 GHz, and 1.91 GHz are indicated by the grey dash line. The most evident variation is in peak 2, represented more closely in figure 18b.

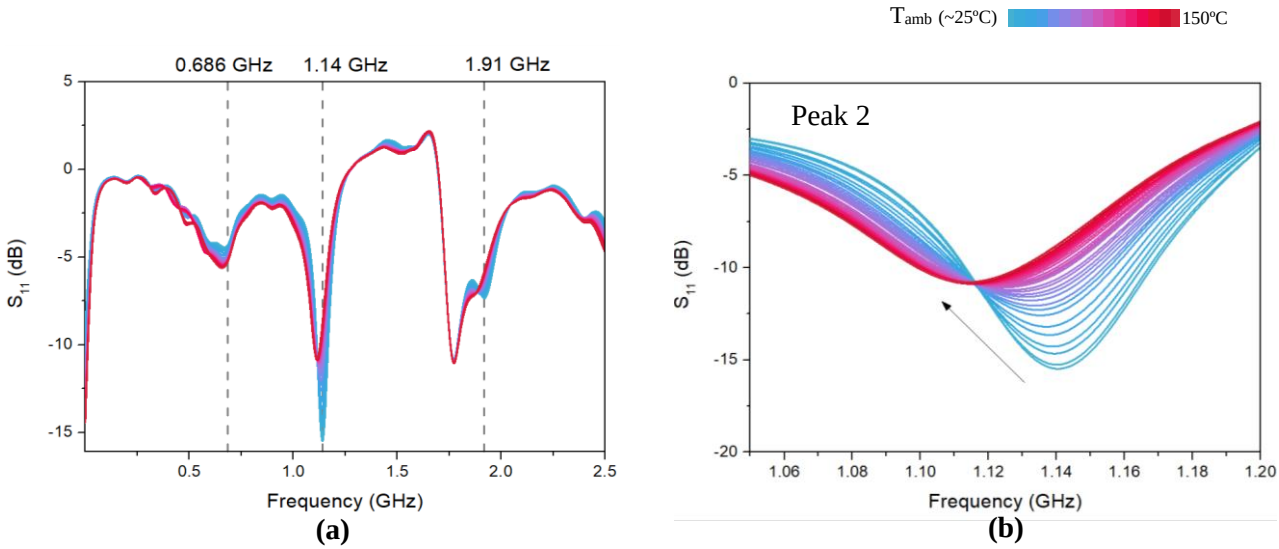

Figure 18 – **(a)** Graph of the behavior of the sensor when a temperature variation is applied. The 3 resonant peaks are identified with a grey dash line **(b)** Graph of peak 2 of the sensor when a temperature variation is applied. The arrow points to the movement of the peak. The resonant peak shifts to lower frequencies. In this case, a hot plate was put on 150ºC, and each line of the graph was taken by 5 seconds apart, with 30 measurements in total.

From figure 18b, peak 2 (at approximated 1.14 GHz at ambient temperature), is the one where a change in frequency is clearer. The resonant peak shifts to lower frequencies, from 1.14 GHz to near 1.10 GHz. Even though is observed a change in peaks 1 and 3, that change is very difficult to quantify due to those peaks not being as well defined as peak 2.

To quantify this change in frequency with temperature, a thermocouple was used to obtain the temperature of the sensor being analyzed. Although not the most accurate method, it was the only one currently available that could be used in combination with the network analyzer.

From the analysis of peak 2 in figure 19, it is observed that with increasing temperature, the frequency associated with peak 2 decreases. This decrease can be explained by the fact that copper resistance increases with increasing temperature [39], and according to equation 4, the greater the resistance, the lower the resonant frequency. To acquire the sensitivity of the sensor, from peak 2, a plot relating the frequency of the peak with temperature was made (figure 19b). After, a linear fit is done to obtain the equation (type y = mx + b). The slope of the equation corresponds to the sensitivity of the sensor, with units of GHz/ºC.

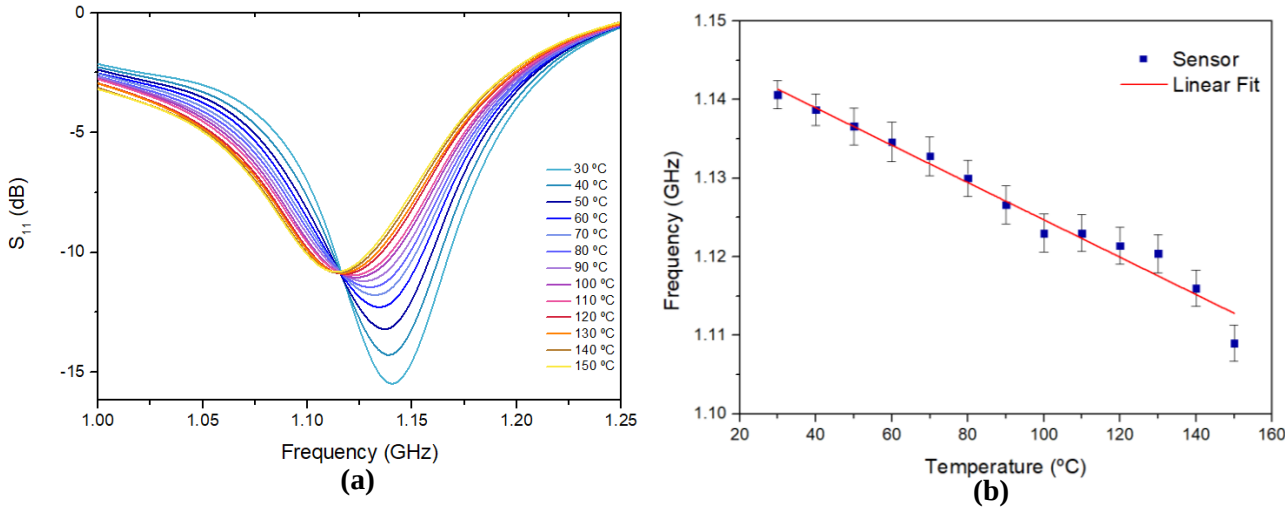

Figure 19 – **(a)** Frequency –S_{11} response curve when the sensor was heated from 30ºC to 150ºC. **(b)** Temperature-Frequency plot of the sensor.

The value of sensitivity for the sensor is, according to the graph in figure 19b, - 0.245 MHz/ºC, although it is important to notice that the error bars along the graph are overlapping, which should be a signal that more samples should be analyzed in the future to reduce the error.

3.2.3 The resonance frequency of the sensor with electrolyte

After the initial analysis of the sensor with temperature, the next step was to cast electrolyte above the sensor, to evaluate how the sensor would behave. The purpose of this is simple, to mimic the inside of a battery. In figure 20, a scheme of the process of casting and a photograph of the sensor with a coating of electrolyte is displayed.

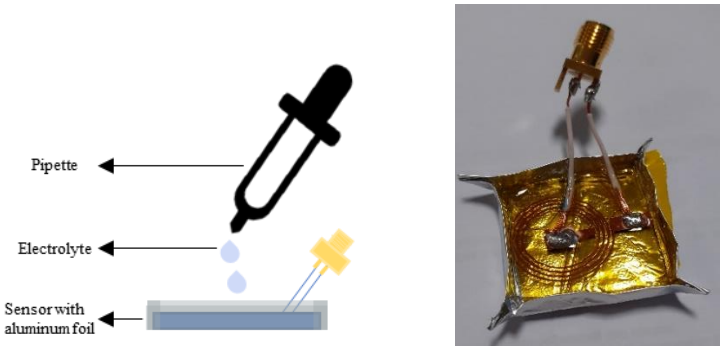

Figure 20 - Sensor with the electrolyte in the process of drying. In the image, it is possible to see the sensor already with the electrolyte on top. The aluminum foil is removed once the drying occurs (after 24 hours). The bottom of the glass substrate is covered with Kapton to facilitate the removal of the aluminum foil.

3.2.3.1 Resonance frequency at ambient temperature

After the casting of the electrolyte on top of the sensor, is important to examine how the resonance peaks change. In figure 21 are presented the graphs for the sensor before the casting of the electrolyte, after 24, 48, and 72 hours.

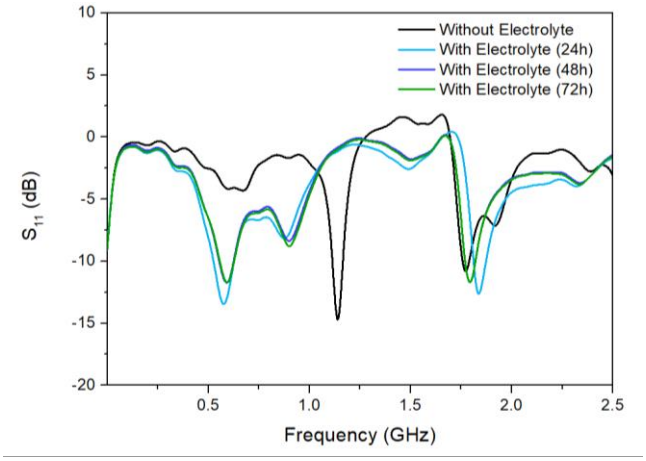

Figure 21 – Frequency response of the sensor before the electrolyte casting on top of the sensor, 24, 48, and 72 hours after the casting.

As seen in the graph of figure 21, the change between the 48h and 72h is almost unnoticeable, unlike what is observed between the 24h and 48h. For this reason, the temperature analysis of the sensor with the electrolyte was only performed after 72h, to make sure that the resonance response was stabilized.

After 72h, peak 2 that was analyzed previously in section 3.2.2 (1.14 GHz) disappeared, but another at 0.96 GHz emerged. Also, peak 1 shifted from a frequency value of 0.68 GHz to 0.61 GHz

Equation (4) referred to in section 3.1.1, which demonstrates the parameters with which the resonance frequency is defined, could help in forming an explanation on why these changes occurred in the peaks after electrolyte deposition, and over the next 72 hours. The sensor capacity influences the resonance frequency, and in turn, the dielectric constant of the medium influences the sensor capacity, as shown in equation 6:

$$C = \frac{\varepsilon_0 \, \varepsilon_r \, S}{d} \tag{6}$$

C – Capacitance (F);
ε_0 - Permittivity of vacuum (F/m);
ε_r – Relative permittivity;
S – Area of facing electrodes (m^2);
d – Distance between electrodes (m).

Placing the electrolyte on the sensor will cause the dielectric constant of the medium to change, which could affect the resonance peaks. With dielectric constants such as 3 for PMMA [40], 7.36 for THF [41], and 89.78 for EC [42] (at a temperature of 25ºC), the capacity of the sensor will increase, and with that, the resonance frequency also shifts. On table 5 are displayed the frequency values for each peak.

To summarize, there are two important phenomena that the previous graph show. The first is that when placing the electrolyte in the sensor, the peaks will shift due to the dielectric constant of the medium also changing, as explained previously. The second is that the evaporation of the solvent (THF) could be the factor that is causing the small shift in the first 48h after the sensor being in contact with the electrolyte.

Table 5 – Resonance peaks after the electrolyte covers the sensor.

	Peak Nº	Frequency [GHz]	Deviation
24 h	1	0.57	±0.02
	2	0.91	±0.02
	3	1.85	±0.04
48 h	1	0.61	±0.02
	2	0.93	±0.03
	3	1.84	±0.03
72 h	1	0.62	±0.02
	2	0.93	±0.03
	3	1.84	±0.03

3.2.3.2 First temperature measurement with electrolyte

The first temperature measurement of the sensor with the electrolyte was carried out after 3 days. Looking at the graph in figure 22a, the peak at 0.61 GHz is the one that more prominent shifts, as seen closely in figure 22b. This peak shows different behavior in comparison with the results exhibited earlier for the sensor without the electrolyte since in that case peak 2 was the one that had a more prominent shift. In the overall graph, there is an evident shift in all the frequency responses of the sensor (except the peak at 1.77 GHz).

In this case, the sensor with electrolyte does not have a linear behavior for the 0.61 GHz peak, as it was without the electrolyte (figure 19). To comprehend better how the frequency of this peak changes with temperature, plots from 30ºC to 150ºC were analyzed further ahead.

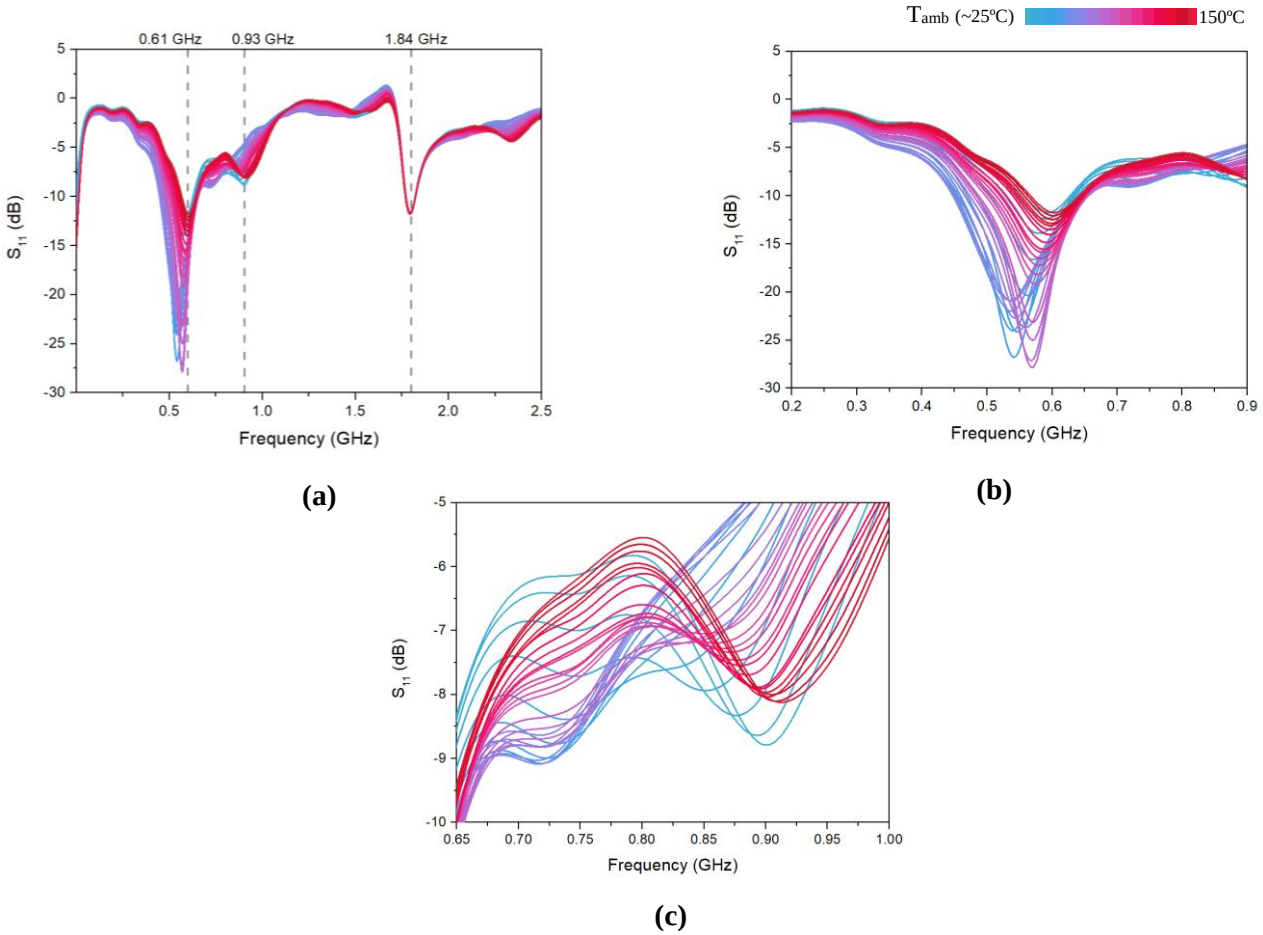

Figure 22 – **(a)** Behaviour of the sensor with electrolyte on top. **(b)** A closer look at the peak 1 at 0.61 GHz. **(c)** A closer look at the peak 2 at 0.93 GHz

Of all the three peaks, only peak 1 was analyzed more deeply, due to peak 2 not being well defined (as seen in figure 22c), and peak 3 not having a shift with temperature.

In figure 23 is shown how it was the physical aspect of the electrolyte in the sensor before and after the first measurement with temperature. As observed, after reaching 150ºC, the electrolyte had formed bubbles. Those bubbles were formed probably due to the solvent that was still in the electrolyte. The formation of these bubbles could potentially affect the following measurements.

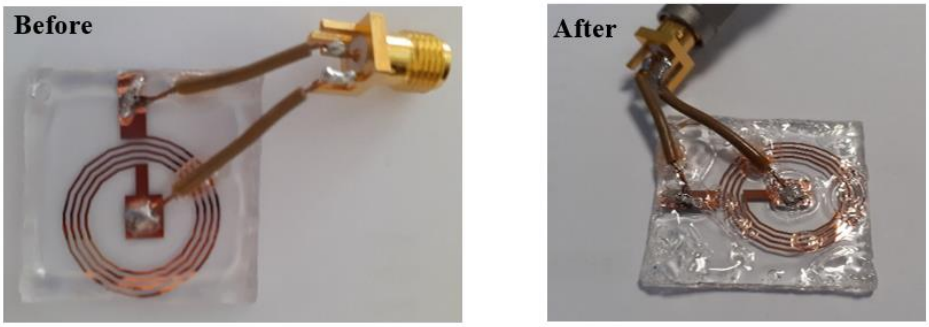

Figure 23 - The sensor before and after the first measurement with temperature.

Regarding the response of the sensor shown in figure 24a, as referred before, the response is not linear. Between 30ºC and 70ºC, the frequency of the peak decreases as expected (since the resistance of the copper increases with temperature). But from 70 ºC to 150 ºC the sensor has an opposite behavior, as the resonance peak shifts to the right. This different behavior is confirmed by the plot in figure 24b. These results could be the indication that the THF solvent plays a role in the sensor behavior since it has a boiling temperature of 66ºC [43], and as seen, when that temperature was reached, the behavior of the sensor changed.

The calculation of the sensitivity of the sensor from peak 1 was made by dividing the graph in figure 24b into two parts. The first part (from 30 to 70ºC) showed a sensitivity of -1.54 MHz/ºC, but after the 70ºC the sensitivity is + 0.781 MHz/ºC.

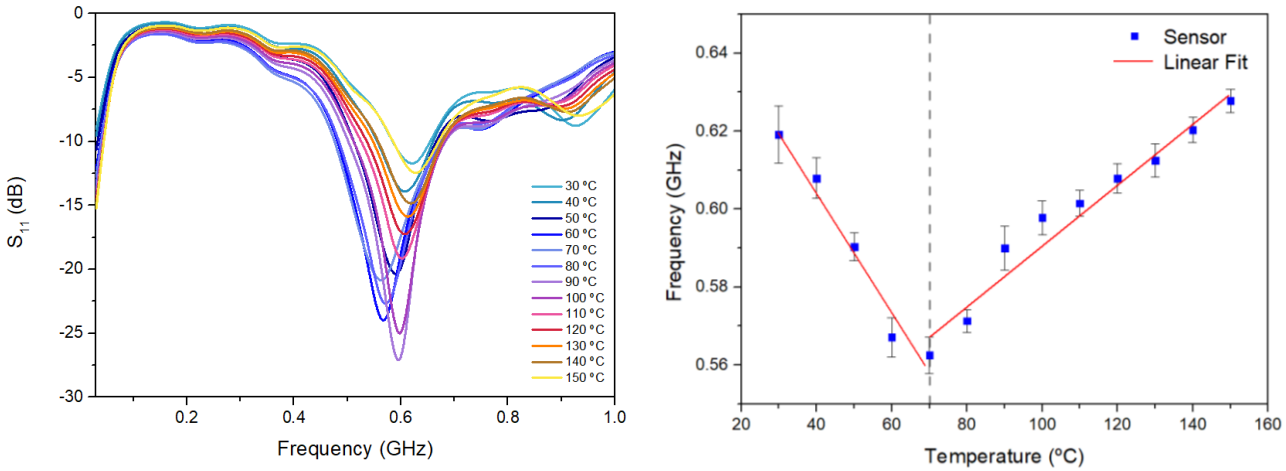

Figure 24 – **(a)** Frequency –S_{11} response curve when the sensor with the electrolyte was heated from 30ºC to 150ºC. **(b)** Temperature-Frequency plot of the sensor.

3.2.3.3 Following temperature measurements

After the first measurement with the temperature reaching 150ºC, measurements after one week, and then after two weeks were taken to see what would be the response that the sensor would give. The peaks 1 and 2 will be further analyzed, the peak 3 will not be studied closer due to the change in the frequency of the peak being almost imperceptible. For the next analysis, it was chosen to obtain the sensitivity of the sensor between 25 ºC and 110ºC, due to the change in frequency above the 110 ºC being not as noticeable as it was for lower temperatures.

1 week after

One week after the first measurement, an interesting point is that the resonance peaks appear similar to the values before the casting of the electrolyte. As seen in figure 25a, in comparison with the graph obtained at section 3.2.3.2, the peak that now has more amplitude is at 1.05 GHz, as opposed to the graph in figure 23a, which had a small peak near 0.93 GHz.

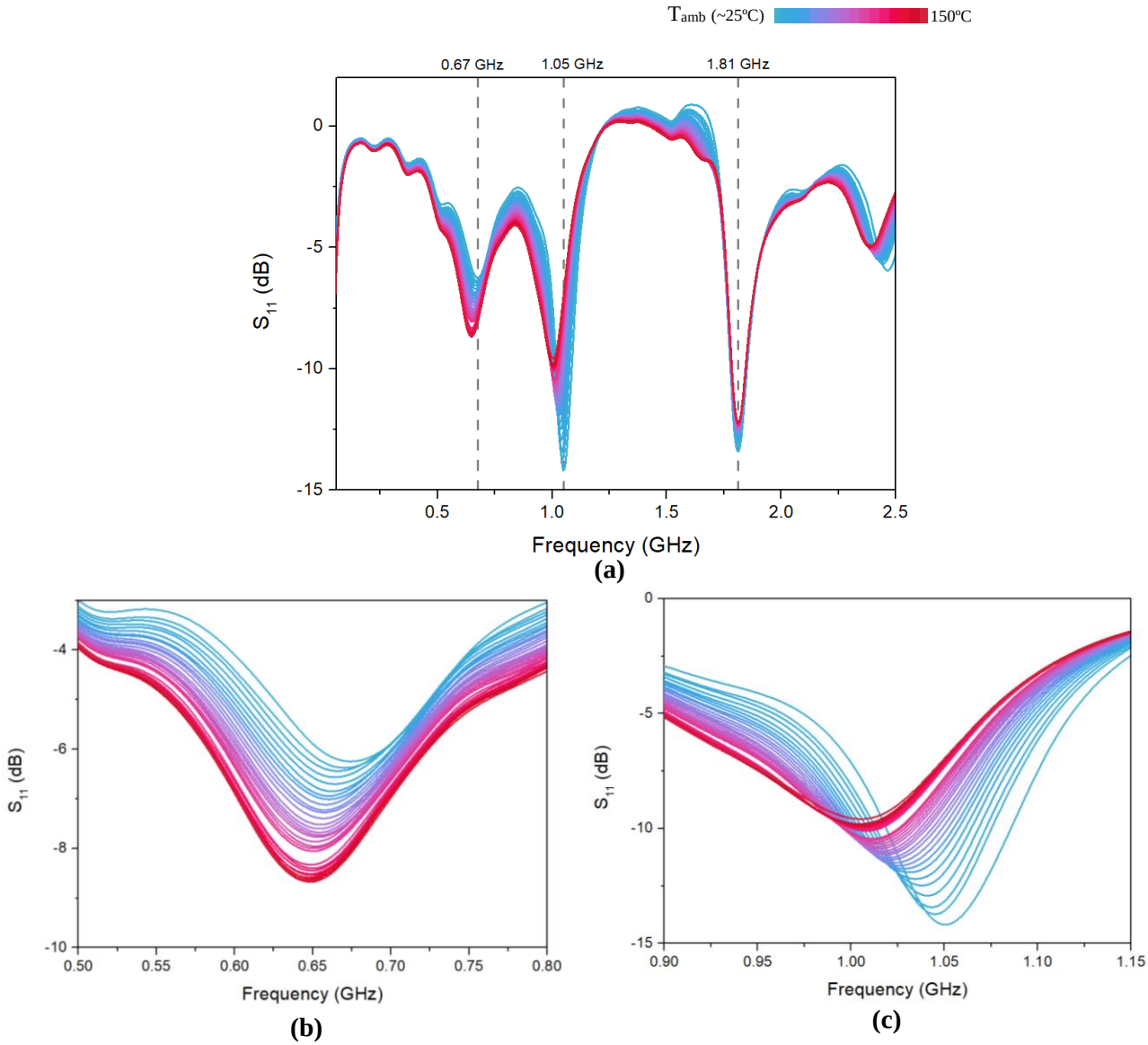

Figure 25 - **(a)** Temperature response curve. **(b)** Close-up view of the temperature response curve for peak 1 (0.67 GHz). **(c)**Close-up view of the temperature response curve for the peak at near 1.05 GHz.

1ºPeak – 0.70 GHz

For a better understanding of why the behavior of the sensor is different one week after the first temperature measurement, a closer look at the response of peak 1 and peak 2 is necessary.

The results for peak 1, in figure 26, show that the frequency of the peak reduces with the increasing temperature, but, especially for temperatures above 100ºC, the shift is almost imperceptible. For that reason, results for sensitivity obtained by the linear fit in figure 26b are not meaningful (sensitivity of 0.264 MHz/ºC)

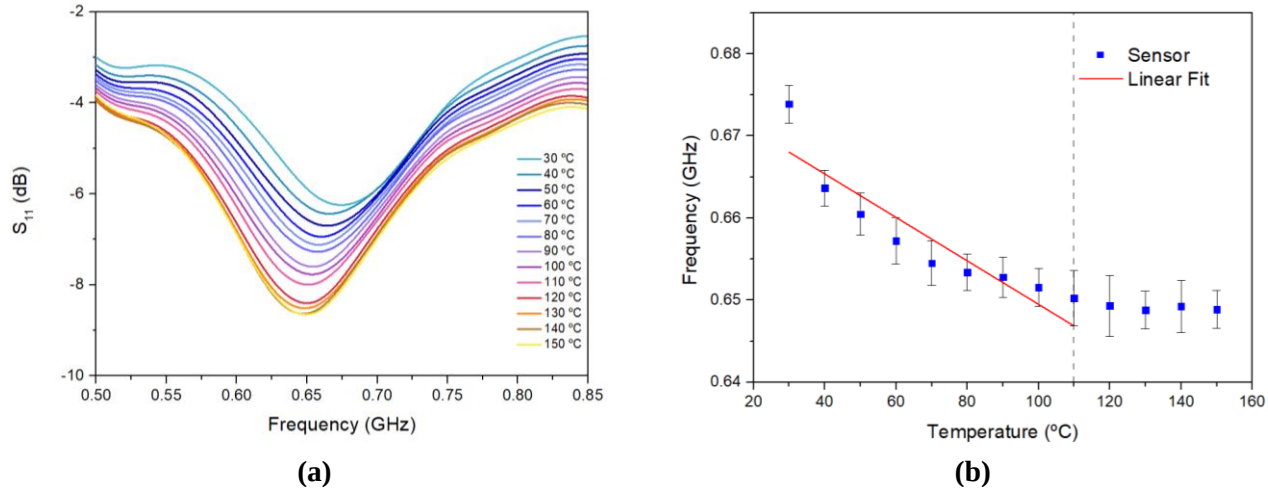

(a) **(b)**

Figure 26 – **(a)** Frequency –S_{11} response curve when the sensor with the electrolyte was heated from 30ºC to 150ºC. **(b)** Temperature-Frequency plot of the sensor.

2º Peak – 1.05 GHz

A closer look at the response of peak 2 to increased temperature, after one week, is displayed in figure 27. The results, particularly in figure 27b, show that the resonance frequency decreases with the increased temperature.

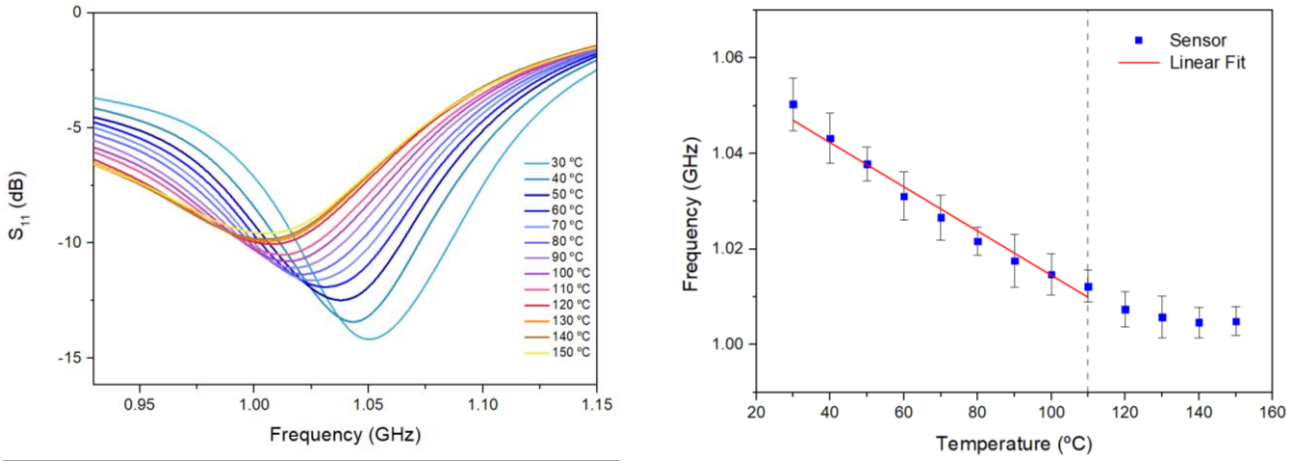

(a) **(b)**

Figure 27 - (a) Frequency –S_{11} response curve when the sensor with the electrolyte was heated from 30ºC to 150ºC. **(b)** Temperature-Frequency plot of the sensor.

Comparing peak 1 with peak 2 after one week, it is obvious that peak 2 has better sensitivity, with - 0.461 MHz/ºC. This result contributes to the hypothesis that peak 2 is the best peak to sense temperature variations.

2 weeks after

The results of the measurements performed two weeks after the casting of the electrolyte can be observed in figure 28. After two weeks of being in contact with the electrolyte, the sensor shows a different behavior compared with the previous measurements performed, since it looks as if all the graph is shifting, and not just the peaks, as noticeable in figure 28a.

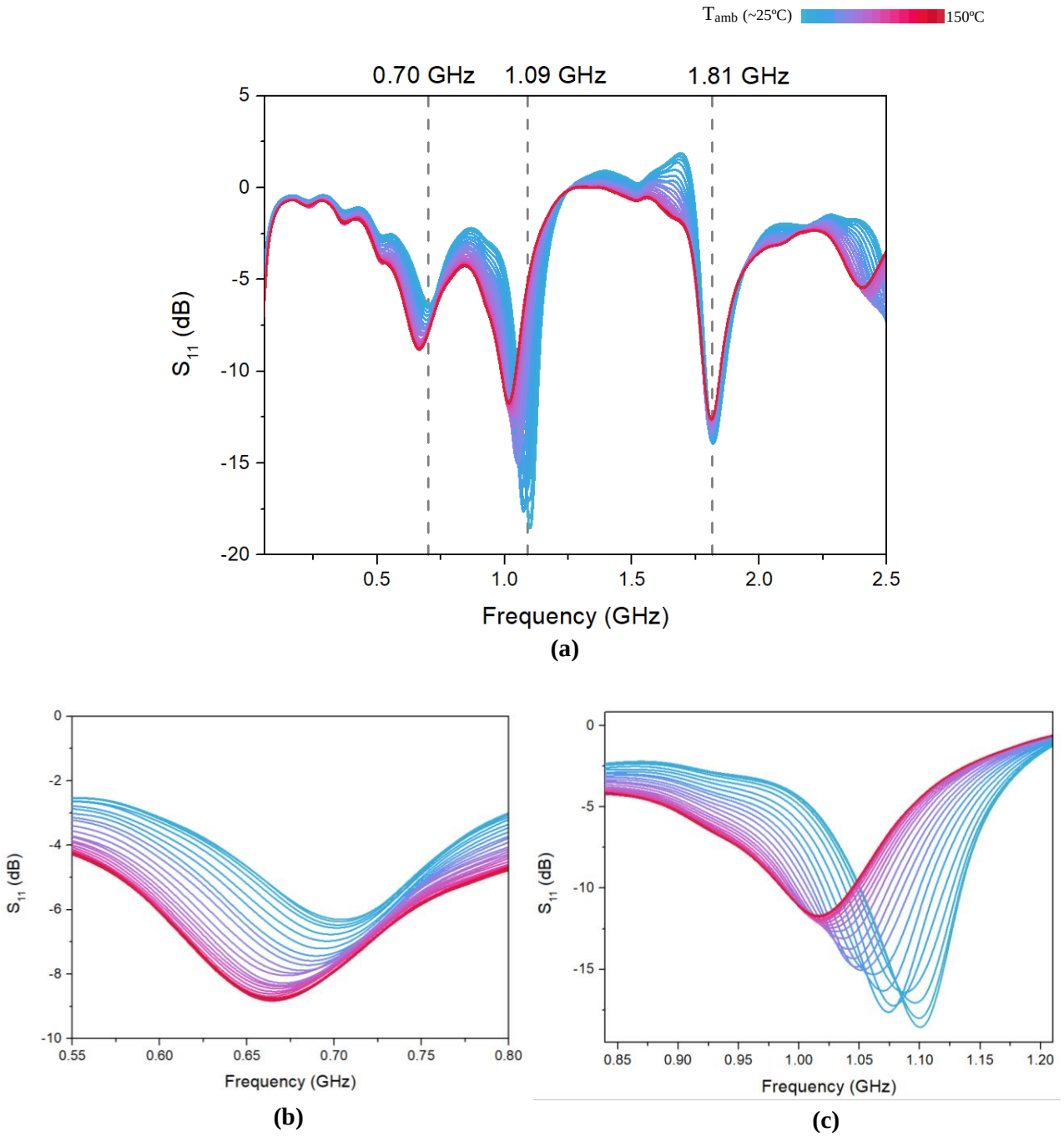

Figure 28 – **(a)** Frequency vs. S_{11} curve of the sensor after 2 weeks with a temperature sweep. **(b)** Close-up of the resonance peak 1 **(c)** Close-up of the resonance peak 2.

1ºPeak – 0.70 GHz

A closer look at the response of peak 1 after two weeks is displayed in figure 29. The most noticeable aspect of the graph in figure 29b is that after the sensor reaches 110 ºC, the change in the resonant frequency is almost unnoticeable. The sensitivity determined was - 0.554 MHz/ºC.

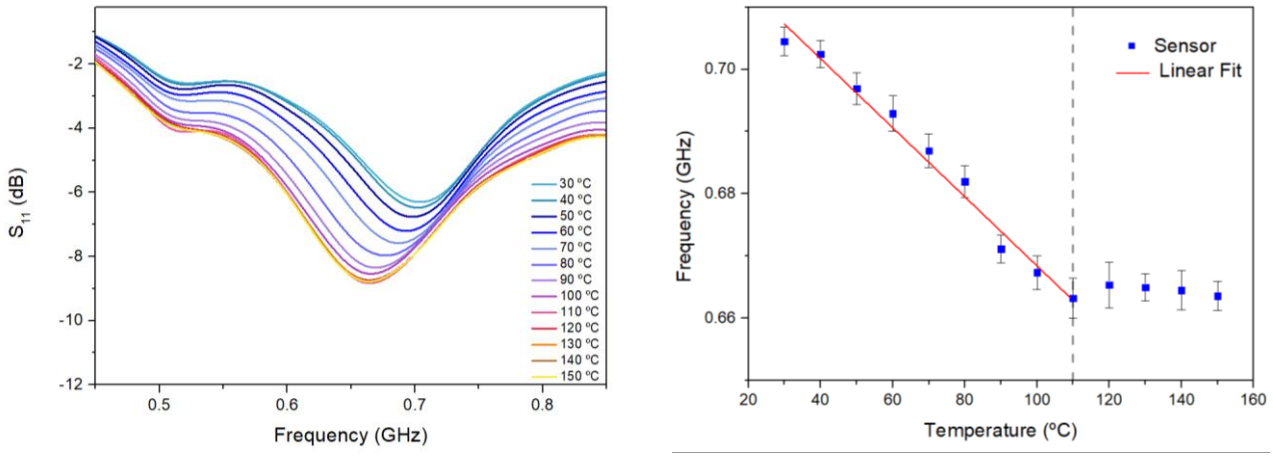

(a) **(b)**

Figure 29 – **(a)** Frequency –S_{11} response curve when the sensor with the electrolyte was heated from 30ºC to 150ºC. **(b)** Temperature-Frequency plot of the sensor.

2º Peak – 1.09 GHz

The response of peak 2 after two weeks is displayed in figure 30. From the graph in figure 30b, an obvious distinction between the sensor behavior between 30ºC and 110 ºC, and after the 110 ºC is presented, similar to what happened for peak 1. From 30ºC to 110ºC the sensitivity is - 1.18 MHz/ºC.

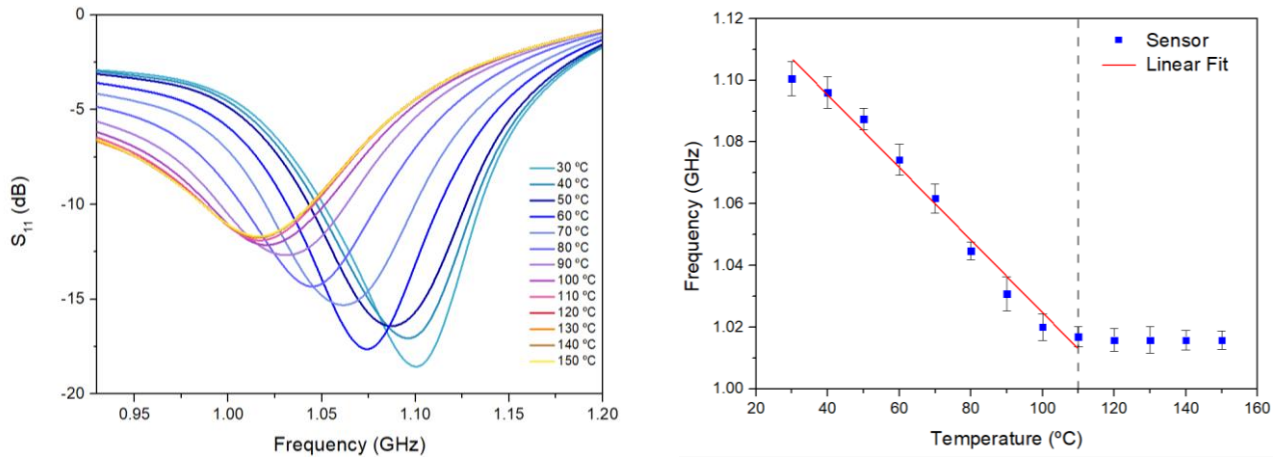

(a) **(b)**

Figure 30 - **(a)** Frequency –S_{11} response curve when the sensor with the electrolyte was heated from 30ºC to 150ºC. **(b)** Temperature-Frequency plot of the sensor.

After obtaining the results of one and two weeks after the first measurement of the sensor with the electrolyte, it is necessary to compare results and discuss why the results differed. In table 6 are presented the results of peaks 1 and 2 after one and two weeks.

Table 6 – Peaks 1 and 2 after one and two weeks.

	Peak 1 [GHz] at 25ªC	Sensitivity [MHz/ºC]	Peak 2 [GHz] at 25ºC	Sensitivity [MHz/ºC]
1 week after	0.68 ± 0.02	- 0.264	1.05 ± 0.03	- 0.461
2 weeks after	0.70 ± 0.02	- 0.554	1.08 ± 0.02	- 1.18

Comparing the values of frequency for peaks 1 and 2, obtained one and two weeks after, it shows that the resonance peaks change position, which could be explained by the fact that every time that the sensor with the electrolyte is heated until 150 ºC, some type of degradation happens, as seen in figure 31, where it is apparent that the electrolyte is full of bubbles and even has some white parts.

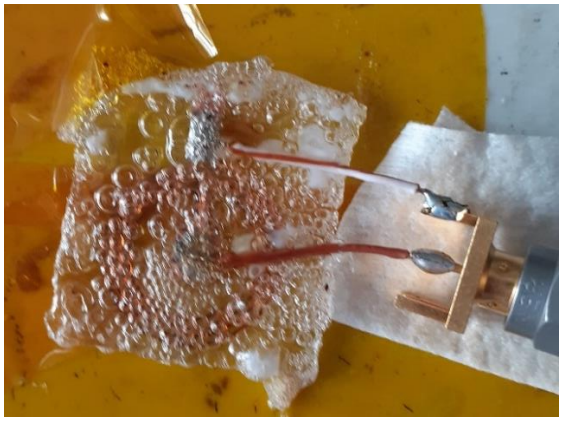

Figure 31 – Aspect of the sensor with the electrolyte after 2 weeks and 3 measurements with temperature.

Also, another conclusion that can be drawn is that the sensitivity of peak 2 is greater than the one for peak 1, both after a week and after two. These results demonstrate that for future studies using this sensor, the analysis should be focused on peak 2. Although the response of the sensor in the first temperature measurement should be investigated to understand if the THF solvent is the one causing the abnormality in the first results.

Analizing the results obtained after the first week, not only the electrolyte degradation could be a factor influencing these results, but also the copper (the material used for the sensors) could be affected by being in contact with the electrolyte, and thus affecting the measurements.

The change of behavior of the sensor after one week, (second measurement with temperature), can be an indication that the glass transition temperature of the PMMA or/and the humidity influences the sensor's response, and that after the first measurement with the temperature reaching 150ºC, the polymers that compose the electrolyte change in some way that affects the resonance frequency. As displayed in table 7 (Annex 1) PMMA has a glass transition temperature at 105 ºC, which is a temperature that is met and exceeded in the first temperature measurement that was obtained with the electrolyte.

Another important point is the humidity, since all the tests were performed with humidity at approximated 45%, that percentage of humidity could influence the response of the sensor since the electrolyte is composed of PMMA and $LiCF_3SO_3$. And according to Ito et al. [44], which investigated the effects of $LiCF_3SO_3$ on the glass transition temperature (T_g) of PMMA, under dry conditions the T_g was greatly enhanced by the lithium salt, but, when the PMMA containing $LiCF_3SO_3$ was exposed to humidity, a large amount of water was absorbed, and as a result, the T_g shifted to a lower temperature.

4 Conclusion and Future Perspectives

4.1 Final Conclusions

To fabricate a safe Li-S battery is important to have a way to measure the internal temperature inside the battery. In this work, it was proposed a device that can sense changes in temperature from the change in the resonance frequency of the sensor. Since the final goal was to incorporate the sensor inside a battery, one of the focal points of this work was to comprehend how the sensor behaved when incorporated with an electrolyte.

RLC sensors were were designed in KLAYOUT and, fabricated in copper and titanium. The first analysis of the sensor subject to increased temperature showed that peak 2 decreased frequency. This behavior could be justified due to the copper increasing the resistance with increasing temperature, and for an RLC circuit, when the resistance increases, the resonance frequency decreases.

Following the first analysis, assessing the performance of the sensor with the electrolyte was the next step. In the first temperature measurement with electrolyte, we observed a peak at near 0.61 GHz. The response of the resonance frequency peak was not linear. Between 30ºC and 70ºC, the frequency of the peak decreases, but from 70 ºC to 150 ºC the sensor has an opposite behavior, as the resonance peak increases. These results could be the indication that the THF solvent plays a role in the sensor behavior since it has a boiling temperature of 66ºC [43].

Then, two more measurements were made, one week and then two weeks after. After one week both peaks 1 and 2 showed a linear behavior since the frequency of the peaks decreased with the increasing temperature. Although that for temperatures above 110 ºC the sensitivity of the sensor was not as noticeable as it was for lower temperatures (<110ºC), the reason why it was chosen to only obtained the sensitivity between the 25 ºC and 110 ºC .

Next, the temperature measurement after two weeks clearly showed that for temperatures above 110ºC the response of the sensor was weak. As discussed before, the performance of the sensor, and these results, could be influence by some factors such as humidity, degradation of not only the electrolyte but also the sensor.

For this sensor, although three distinct peaks were identified, peak 2, between 0.93 and 1.16 GHz, was the one that proved to be the most promising to be used in temperature measurement, due to its greater sensitivity compared to the other two. Peak 2 demonstrated a sensitivity of - 0.461 MHz/ºC and – 1.18 MHz/ºC , after a week and two weeks, respectively.

This work faced some obstacles, the main one being the equipment used to obtain the peaks of the resonance frequency. The network analyzer used in this work could only store data in a floppy disk, which is

very unreliable and extremely sensitive to magnetic fields. These disadvantages meant that even with great care, some of the data obtained could not be analyzed as it was damaged.

Using a more precise method to obtain the temperature will be helpful to have a precise value of frequency for each of the temperatures.

This work would benefit if it had been possible to analyze the data regarding the variation of inductance/capacity/resistance in relation to temperature, in order to have a more solid idea of how these parameters vary in the sensor when there is temperature variation. The main objective of this thesis, which was to test whether the temperature sensor would work, was fulfilled.

4.2 Future Perspectives

With the increasing modernization of the world in which we live, the evolution of batteries is one of the most important requirements. Li-S batteries can meet the demands of the market, but in addition to their energy storage capacity, their safety is also imperative. Having a passive system that allows us to monitor what is going on inside the battery, namely inside the electrolyte, is extremely vital.

The sensors manufactured and studied in this work can be the first step towards a system to check in real-time how changes are happening inside a battery. But to achieve the final objective, many steps must be optimized, namely concerning the fabrication of both the sensor and its analysis.

Starting with the sensor design, a study must be done to understand how to achieve a sensor that presents very well-defined resonance peaks, so that it is possible to identify them without a doubt. The range for the operating frequencies desired must be stipulated, and with that, parameters such as the width and thickness of the lines, the space between them, and the general dimensions of the sensor must be chosen. Smaller sensors will mean that the range of operating frequencies will be higher (in the GHz).

After having a well-established design, the next step could be the choice of the materials that can be used to fabricate the sensors. In this work, a layer of 20 nm of titanium was deposited on a glass substrate to improve the adhesion of the 200 nm layer of copper that will constitute the sensor. Other materials should be investigated since copper is a relatively easy material to oxidize with time. To surpass that problem, a logical element to choose could be gold. Another aspect to take into account is how the material that composes the sensor behaves in the presence of the electrolyte since many compounds used in the formulation of the electrolyte can cause some form of degradation on the sensor.

Investigate other substrates for the sensor is also an important point, changing from glass to parylene or kapton can be an interesting choice.

As for the electrolytes, a study must be conducted to understand the impact on the behavior of the sensor when electrolytes with another formulation are used. As discussed earlier in the introduction, several other polymers can be used, such as PEO, PAN, and PVdF. Being able to control with precision the thickness of the electrolyte is also relevant, considering that this could influence the frequency response of the sensor. The concentration of lithium-ions is also an important matter, being that one of the points debated in the discussion was if the lithium-ions were the reason for the shift in the frequency response of the sensors.

Another point worth mentioning is to make the measurements of the operating frequencies of the sensors more reliable. In this work, intermediate cables were used to connect the sensor to the SMA connector, which in turn connected to the Port 1 cable of the Network Analyzer. Unfortunately, in the welding process, due to the thin thickness of the sensors, some ended up damaged and unusable. Finding a solution (such as the one presented in figure 34) that would allow discarding the wires that have to be welded to the sensors would not only facilitate the analysis but also withdraw a factor that can make the readings of the resonance frequencies less reliable.

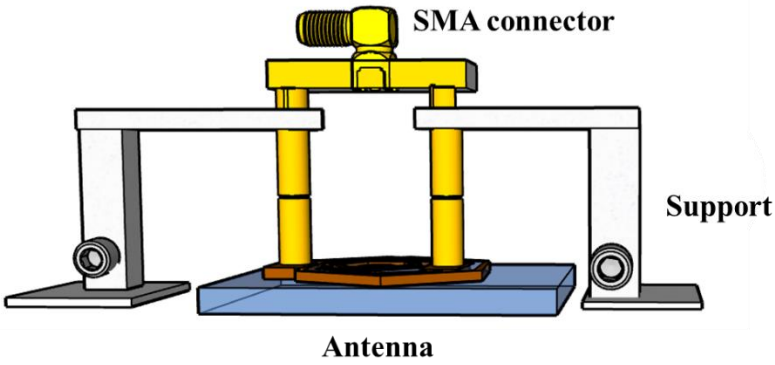

Figure 32- Idea for a support that can be used to analyze the sensor.

As referred before, one of the biggest difficulties of this work was using a network analyzer that only could store data in floppy disks, which brought obstacles since they demagnetize very easily, often leading to data being damaged and unable to be retrieved. For future work hopefully using equipment that stores data in a USB-drive for example can make the work more efficient.

Overall, for this project to succeed in its ultimate goal, there must be a good association between the electrolyte, the sensor, and the analysis process.

5 References

[1] P. G. Bruce, “Energy storage beyond the horizon: Rechargeable lithium batteries,” *Solid State Ionics*, vol. 179, no. 21–26, pp. 752–760, 2008.

[2] X. Ji and L. F. Nazar, “Advances in Li-S batteries,” *J. Mater. Chem.*, vol. 20, no. 44, pp. 9821–9826, 2010.

[3] L. F. Nazar, M. Cuisinier, and Q. Pang, “Lithium-sulfur batteries,” *MRS Bull.*, vol. 39, no. 5, pp. 436–442, 2014.

[4] K. J. Siczek, “Introduction to Lithium-Sulfur Batteries,” *Next-Generation Batter. with Sulfur Cathodes*, pp. 5–13, 2019.

[5] Y. X. Yin, S. Xin, Y. G. Guo, and L. J. Wan, “Lithium-sulfur batteries: Electrochemistry, materials, and prospects,” *Angew. Chemie - Int. Ed.*, vol. 52, no. 50, pp. 13186–13200, 2013.

[6] U. Zubair, J. Amici, C. Francia, D. McNulty, S. Bodoardo, and C. O’Dwyer, “Polysulfide Binding to Several Nanoscale Magnéli Phases Synthesized in Carbon for Long-Life Lithium–Sulfur Battery Cathodes,” *ChemSusChem*, vol. 11, no. 11, pp. 1838–1848, 2018.

[7] S. S. Zhang, “Liquid electrolyte lithium/sulfur battery: Fundamental chemistry, problems, and solutions,” *J. Power Sources*, vol. 231, pp. 153–162, 2013.

[8] Q. Yang, N. Deng, J. Chen, B. Cheng, and W. Kang, “The recent research progress and prospect of gel polymer electrolytes in lithium-sulfur batteries,” *Chem. Eng. J.*, no. October, p. 127427, 2020.

[9] Z. Zhuang, Q. Kang, D. Wang, and Y. Li, “Single-atom catalysis enables long-life , high-energy lithium – sulfur batteries,” vol. 13, no. 7, pp. 1856–1866, 2020.

[10] B. Liu *et al.*, “Revisiting Scientific Issues for Industrial Applications of Lithium-Sulfur Batteries,” *Energy Environ. Mater.*, vol. 1, no. 4, pp. 196–208, 2018.

[11] M. Yuriy and I. Kovalev, “High Energy Rechargeable Li-S Cells for EV Application: Status, Remaining Problems and Solutions,” *ECS Trans.*, vol. 25, no. 35, pp. 23–34, 2010.

[12] X. Chen, T. Hou, B. Li, C. Yan, L. Zhu, and C. Guan, “Towards stable lithium-sulfur batteries : Mechanistic insights into electrolyte decomposition on lithium metal anode,” vol. 8, no. October 2016, pp. 194–201, 2017.

[13] W. Wang *et al.*, “The electrochemical performance of lithium-sulfur batteries with LiClO 4 DOL/DME electrolyte,” *J. Appl. Electrochem.*, vol. 40, no. 2, pp. 321–325, 2010.

[14] N. Boaretto, L. Meabe, M. Martinez-Ibañez, M. Armand, and H. Zhang, "Review—Polymer Electrolytes for Rechargeable Batteries: From Nanocomposite to Nanohybrid," *J. Electrochem. Soc.*, vol. 167, no. 7, p. 070524, 2020.

[15] S. Zhang, K. Ueno, K. Dokko, and M. Watanabe, "Recent Advances in Electrolytes for Lithium – Sulfur Batteries," pp. 1–28, 2015.

[16] X. Huang *et al.*, "Comprehensive evaluation of safety performance and failure mechanism analysis for lithium sulfur pouch cells," *Energy Storage Mater.*, vol. 30, no. April, pp. 87–97, 2020.

[17] M. Ue, K. Sakaushi, and K. Uosaki, "Basic knowledge in battery research bridging the gap between academia and industry," *Mater. Horizons*, vol. 7, no. 8, pp. 1937–1954, 2020.

[18] M. M. Titirici, "Sustainable Batteries—Quo Vadis?," *Adv. Energy Mater.*, vol. 2003700, pp. 1–11, 2021.

[19] L. Huang *et al.*, "Electrode Design for Lithium–Sulfur Batteries: Problems and Solutions," *Adv. Funct. Mater.*, vol. 30, no. 22, pp. 1–30, 2020.

[20] Y. Feng *et al.*, "Towards high energy density Li–S batteries with high sulfur loading: From key issues to advanced strategies," *Energy Storage Mater.*, vol. 32, no. April, pp. 320–355, 2020.

[21] E. S. D.-I. Stroea, V. Knapa, M. Swierczynskia, "Thermal Behavior and Heat Generation Modeling of Lithium Sulfur Batteries," vol. 77, no. 11, pp. 467–476, 2017.

[22] A. Bhargav, J. He, and A. Gupta, "Lithium-Sulfur Batteries : Attaining the Critical Metrics," *Joule*, pp. 1–6, 2020.

[23] X. Huang, M. Xiao, D. Han, J. Xue, S. Wang, and Y. Meng, "Thermal runaway features of lithium sulfur pouch cells at various states of charge evaluated by extended volume-accelerating rate calorimetry," *J. Power Sources*, vol. 489, no. January, p. 229503, 2021.

[24] Z. Kailong, LIU; Kang, LI; Qiao PENG; Cheng, "A brief review on key technologies in the battery management system of electric vehicles," vol. 14, no. 1, pp. 47–64, 2019.

[25] S. Goutam, J. Timmermans, N. Omar, P. Van Den Bossche, and J. Van Mierlo, "Comparative Study of Surface Temperature Behavior of Commercial Li-Ion Pouch Cells of Different Chemistries and Capacities by Infrared Thermography," pp. 8175–8192, 2015.

[26] Y. Tripathy, A. Mcgordon, J. Low, and J. Marco, "Internal Temperature Prediction of Lithium-ion Cell Using Differential Voltage Technique," pp. 464–467, 2017.

[27] M. Nascimento *et al.*, "Internal strain and temperature discrimination with optical fiber hybrid sensors in Li-ion batteries," *J. Power Sources*, vol. 410–411, no. October 2018, pp. 1–9, 2019.

[28] J. Philipp, S. Arnold, A. Loges, D. Werner, T. Wetzel, and E. Ivers-tiffée, "Measurement of the internal cell temperature via impedance : Evaluation and application of a new method," *J. Power Sources*, vol. 243, pp. 110–117, 2013.

[29] N. A. David, P. M. Wild, J. Hu, and N. Djilali, "In-fibre Bragg grating sensors for distributed temperature measurement in a polymer electrolyte membrane fuel cell," *J. Power Sources*, vol. 192, no. 2, pp. 376–380, 2009.

[30] J. K. Sahota, N. Gupta, and D. Dhawan, "Fiber Bragg grating sensors for monitoring of physical parameters : a comprehensive review," *Opt. Eng.*, vol. 59, no. June 2020, pp. 1–35, 2021.

[31] D. H. Doughty, P. C. Butler, R. G. Jungst, and E. P. Roth, "Lithium battery thermal models," vol. 110, pp. 357–363, 2002.

[32] S. Novais *et al.*, “Internal and External Temperature Monitoring of a Li-Ion Battery with Fiber Bragg Grating Sensors,” pp. 1–9.

[33] Q. Huang, L. Dong, and L. Wang, “LC Passive Wireless Sensors Toward a Wireless Sensing Platform : Status , Prospects , and Challenges,” *J. Microelectromechanical Syst.*, vol. 25, no. 5, pp. 822–841, 2016.

[34] F. Sanmin, Shen; Zhihong, “An LC Passive Wireless Gas Sensor Based on PANI/CNT Composite,” 2018.

[35] V. Kalinin, “Passive wireless strain and temperature sensors based on SAW devices,” *Proc. - 2004 IEEE Radio Wirel. Conf. RAWCON*, pp. 187–190, 2004.

[36] K. S. V. Idhaiam *et al.*, “Micromachined Ceramic-based Chipless LC Resonator for High-Temperature Wireless Sensing Application in Harsh Environments,” pp. 1–42, 2020.

[37] Y. Wang, Q. Tan, L. Zhang, B. Lin, M. Li, and Z. Fan, “Wireless passive lc temperature and strain dual-parameter sensor,” *Micromachines*, vol. 12, no. 1, pp. 1–10, 2021.

[38] C. C. Sun, A. H. You, and L. L. Teo, “Characterizations of PMMA-based polymer electrolyte membranes with Al2O3,” *J. Polym. Eng.*, vol. 39, no. 7, pp. 612–619, 2019.

[39] J. H. Dellinger, “The temperature coefficient of resistance of copper,” *J. Franklin Inst.*, vol. 170, no. 3, pp. 213–216, 1910.

[40] M. Faridi, L. Naji, S. Kazemifard, and N. Pourali, “Electrochemical investigation of gel polymer electrolytes based on poly(methyl methacrylate) and dimethylacetamide for application in Li-ion batteries,” *Chem. Pap.*, vol. 72, no. 9, pp. 2289–2300, 2018.

[41] N. Gee, K. Shinsaka, and J. Dodelet, “Dielectric temperature constant against for 43 liquids,” 1986.

[42] E. R. Logan, J. Electrochem, A. Soc, L. Y. Beaulieu, and J. R. Dahn, “A Study of the Transport Properties of Ethylene Carbonate-Free Li Electrolytes A Study of the Transport Properties of Ethylene Carbonate-Free Li Electrolytes,” 2018.

[43] K. J. Zeitsch, “D. Properties of tetrahydrofuran,” in *The chemistry and technology of furfural and its many by-products*, vol. 13, K. J. Zeitsch, Ed. Elsevier, 2000, p. 242.

[44] A. Ito, P. Phulkerd, V. Ayerdurai, M. Soga, A. Courtoux, and A. Miyagawa, “Enhancement of the glass transition temperature of poly (methyl methacrylate) by salt,” *Polym. J.*, 2018.

[45] R. Kumar and S. S. Sekhon, “Effect of molecular weight of PMMA on the conductivity and viscosity Effect of molecular weight of PMMA on the conductivity and viscosity behavior of polymer gel electrolytes containing,” no. July 2014, 2008.

[46] X. B. Cheng, J. Q. Huang, Q. Zhang, H. J. Peng, M. Q. Zhao, and F. Wei, “Aligned carbon nanotube/sulfur composite cathodes with high sulfur content for lithium-sulfur batteries,” *Nano Energy*, vol. 4, pp. 65–72, 2014.

[47] A. Manthiram, Y. Fu, and Y. S. Su, “Challenges and prospects of lithium-sulfur batteries,” *Acc. Chem. Res.*, vol. 46, no. 5, pp. 1125–1134, 2013.

[48] M. K. Song, E. J. Cairns, and Y. Zhang, “Lithium/sulfur batteries with high specific energy: Old challenges and new opportunities,” *Nanoscale*, vol. 5, no. 6, pp. 2186–2204, 2013.

[49] H. C. Wang, X. Cao, W. Liu, and X. Sun, “Research Progress of the Solid State Lithium-Sulfur Batteries,” *Front. Energy Res.*, vol. 7, no. October, pp. 1–20, 2019.

[50] Y. Diao, K. Xie, S. Xiong, and X. Hong, “Shuttle phenomenon-The irreversible oxidation mechanism of sulfur active material in Li-S battery,” *J. Power Sources*, vol. 235, pp. 181–186, 2013.

[51] J. Wang *et al.*, “Suppressing the Shuttle Effect and Dendrite Growth in Lithium-Sulfur Batteries,” *ACS Nano*, vol. 14, no. 8, pp. 9819–9831, 2020.

[52] S. Walu *et al.*, “Volumetric expansion of Lithium-Sulfur cell during operation – Fundamental insight into applicable characteristics,” vol. 10, no. June 2017, pp. 233–245, 2018.

[53] C. Weller, J. Pampel, S. Dörfler, H. Althues, and S. Kaskel, “Polysulfide Shuttle Suppression by Electrolytes with Low-Density for High-Energy Lithium–Sulfur Batteries,” *Energy Technol.*, vol. 7, no. 12, pp. 1–12, 2019.

[54] W. Ren, W. Ma, S. Zhang, and B. Tang, “Recent advances in shuttle effect inhibition for lithium sulfur batteries,” *Energy Storage Mater.*, vol. 23, no. February, pp. 707–732, 2019.

[55] M. Wild *et al.*, “Lithium sulfur batteries, a mechanistic review,” *Environ. Sci.*, vol. 6, no. iii, pp. 3477–3494, 2015.

[56] A. Karmakar and A. Ghosh, “Structure and ionic conductivity of ionic liquid embedded PEO- LiCF 3 SO 3 polymer electrolyte,” vol. 087112, no. June 2014, 2015.

[57] W. Li, Y. Pang, T. Zhu, Y. Wang, and Y. Xia, “A gel polymer electrolyte based lithium-sulfur battery with low self-discharge,” *Solid State Ionics*, vol. 318, no. August 2017, pp. 82–87, 2018.

[58] S. S. Jeong *et al.*, “Electrochemical properties of lithium sulfur cells using PEO polymer electrolytes prepared under three different mixing conditions,” *J. Power Sources*, vol. 174, no. 2, pp. 745–750, 2007.

[59] W. Li, Y. Pang, J. Liu, G. Liu, Y. Wang, and Y. Xia, “A PEO-based gel polymer electrolyte for lithium ion batteries,” *RSC Adv.*, vol. 7, no. 38, pp. 23494–23501, 2017.

[60] R. Fang, H. Xu, B. Xu, X. Li, Y. Li, and J. B. Goodenough, “Reaction Mechanism Optimization of Solid-State Li–S Batteries with a PEO-Based Electrolyte,” *Adv. Funct. Mater.*, vol. 31, no. 2, pp. 1–7, 2021.

[61] X. Gu and C. Lai, “Recent development of metal compound applications in lithium-sulphur batteries,” *J. Mater. Res.*, vol. 33, no. 1, pp. 16–31, 2018.

[62] S. Mogurampelly and V. Ganesan, “Effect of nanoparticles on ion transport in polymer electrolytes,” *Macromolecules*, vol. 48, no. 8, pp. 2773–2786, 2015.

[63] B. J. Hassoun and B. Scrosati, “Moving to a Solid-State Confi guration : A Valid Approach to Making Lithium-Sulfur Batteries Viable for Practical Applications,” *Adv. Mater.*, pp. 5198–5201, 2010.

[64] X. Wang, X. Hao, Y. Xia, Y. Liang, X. Xia, and J. Tu, “A polyacrylonitrile (PAN)-based double-layer multifunctional gel polymer electrolyte for lithium-sulfur batteries,” *J. Memb. Sci.*, vol. 582, no. January, pp. 37–47, 2019.

[65] W. Jia *et al.*, “Graphene oxide as a fi ller to improve the performance of PAN-LiClO 4 fl exible solid polymer electrolyte,” vol. 315, no. October 2017, pp. 7–13, 2018.

[66] F. Liu and D. W. Grainger, *Fluorinated Biomaterials*, Third Edit. Elsevier, 2013.

[67] S. Gao *et al.*, “Poly(vinylidene fluoride)-based hybrid gel polymer electrolytes for additive-free lithium sulfur batteries,” *J. Mater. Chem. A Mater. energy Sustain.*, vol. 5, pp. 17889–17895, 2017.

[68] H. Hashim *et al.*, “Natural rubber-grafted with 30% poly(methylmethacrylate) characterization for application in lithium polymer battery,” *CSSR 2010 - 2010 Int. Conf. Sci. Soc. Res.*, no. Cssr, pp. 485–488, 2010.

[69] M. M. Silva, V. D. Z. Bermudez, and A. Pawlicka, “Insight on polymer electrolytes for electrochemical devices applications,” *Polym. Electrolytes Charact. Tech. Energy Appl.*, pp. 113–136, 2019.

[70] U. Ali, K. J. B. A. Karim, and N. A. Buang, “A Review of the Properties and Applications of Poly (Methyl Methacrylate) (PMMA),” *Polym. Rev.*, vol. 55, no. 4, pp. 678–705, 2015.

[71] A. Natarajan, A. M. Stephan, C. H. Chan, N. Kalarikkal, and S. Thomas, “Electrochemical studies on composite gel polymer electrolytes for lithium sulfur-batteries,” *J. Appl. Polym. Sci.*, vol. 134, no. 11, pp. 1–8, 2017.

[72] K. W. Chew, S. S. Chen, W. L. Pang, C. G. Tan, and Z. Osman, “Polymer Electrolytes The Effects of Lithium Triflate (LiCF 3 SO 3) on the PMMA-based Solid Polymer Electrolytes,” vol. 246, no. 2010, pp. 1–6, 2015.

[73] L. H. J. Raijmakers, D. L. Danilov, F. J. Iek-, and D.- Jülich, “A review on various temperature-indication methods for Li-ion batteries,” *Appl. Energy*, vol. 240, no. February, pp. 918–945, 2019.

[74] R. Richardson, “Impedance-based Battery Temperature Monitoring,” no. December, 2016.

[75] A. M. Bizeray, S. Zhao, S. R. Duncan, and D. A. Howey, “Lithium-ion battery thermal-electrochemical model-based state estimation using orthogonal collocation and a modi fi ed extended Kalman fi lter,” *J. Power Sources*, vol. 296, pp. 400–412, 2015.

[76] Q. Wang, P. Ping, X. Zhao, G. Chu, J. Sun, and C. Chen, “Thermal runaway caused fire and explosion of lithium ion battery,” *J. Power Sources*, vol. 208, pp. 210–224, 2012.

[77] X. Hu, S. Member, W. Liu, X. Lin, and Y. Xie, “A Comparative Study of Control-Oriented Thermal Models for Cylindrical Li-Ion Batteries,” vol. 5, no. 4, pp. 1237–1253, 2019.

[78] M. Jozef, D. Loan, and S. Knudsen, “Two-dimensional Thermal Modeling of Lithium-ion Battery Cell Based on Electrothermal Impedance Spectroscopy,” *ECS Trans.*, vol. 72, no. 11, 2016.

[79] K. Murashko and L. Laurila, “Three-Dimensional Thermal Model of a Lithium Ion Battery for Hybrid Mobile Working Machines: Determination of the Model Parameters in a Pouch Cell,” *IEEE Trans. Energy Convers.*, vol. 28, no. 2, 2013.

[80] G. Kim, A. Pesaran, and R. Spotnitz, “A three-dimensional thermal abuse model for lithium-ion cells,” vol. 170, pp. 476–489, 2007.

[81] G. Guo, B. Long, B. Cheng, S. Zhou, P. Xu, and B. Cao, “Three-dimensional thermal finite element modeling of lithium-ion battery in thermal abuse application,” *J. Power Sources*, vol. 195, pp. 2393–2398, 2010.

[82] H. Sun, X. Wang, B. Tossan, and R. Dixon, “Three-dimensional thermal modeling of a lithium-ion battery pack,” *J. Power Sources*, vol. 206, pp. 349–356, 2012.

[83] Y. Kim, S. Mohan, S. Member, J. B. Siegel, A. G. Stefanopoulou, and Y. Ding, “The Estimation of Temperature Distribution in Cylindrical Battery Cells Under Unknown Cooling Conditions,” vol. 22, no. 6, pp. 2277–2286, 2014.

[84] M. Parhizi, M. B. Ahmed, and A. Jain, “Determination of the core temperature of a Li-ion cell during thermal runaway,” *J. Power Sources*, vol. 370, pp. 27–35, 2017.

[85] Y. Kim, J. B. Siegel, and A. G. Stefanopoulou, “A Computationally Efficient Thermal Model of Cylindrical Battery Cells for the Estimation of Radially Distributed Temperatures,” 2013.

[86] Z. Wang, J. U. N. Ma, and L. E. I. Zhang, “Finite Element Thermal Model and Simulation for a Cylindrical Li-Ion Battery,” vol. 5, 2017.

[87] D. Anthony, D. Wong, D. Wetz, and A. Jain, “Non-invasive measurement of internal temperature of a cylindrical Li-ion cell during high-rate discharge,” *Int. J. Heat Mass Transf.*, vol. 111, pp. 223–231, 2017.

[88] S. J. Drake, D. A. Wetz, J. K. Ostanek, S. P. Miller, J. M. Heinzel, and A. Jain, “Measurement of anisotropic thermophysical properties of cylindrical Li-ion cells,” *J. Power Sources*, vol. 252, pp. 298–304, 2014.

[89] N. Martiny and J. Geder, “Development of a Thin-Film Thermocouple Matrix for In-Situ Temperature Measurement in a Lithium Ion Pouch Cell,” *Sensors*, pp. 1–4, 2013.

[90] M. Santosh, K. Mutyala, J. Zhao, J. Li, and H. Pan, “In-situ temperature measurement in lithium ion battery by transferable flexible thin film thermocouples,” *J. Power Sources*, vol. 260, no. August, pp. 43–49, 2014.

[91] G. Yang, C. Leitão, Y. Li, J. Pinto, and X. Jiang, “Real-time temperature measurement with fiber Bragg sensors in lithium batteries for safety usage,” *Measurement*, vol. 46, no. 9, pp. 3166–3172, 2013.

[92] C. E. Campanella, A. Cuccovillo, C. Campanella, A. Yurt, and V. M. N. Passaro, “Fiber Bragg Grating Based Strain Sensors : Review of Technology and Applications,” 2018.

[93] S. J. Mihailov, “Fiber Bragg Grating Sensors for Harsh Environments,” *Sensors*, no. Optical Fiber Sensors, pp. 1898–1918, 2012.

[94] A. Fortier, M. Tsao, N. D. Williard, Y. Xing, and M. G. Pecht, “Preliminary Study on Integration of Fiber Optic Bragg Grating Sensors in Li-Ion Batteries and In Situ Strain and Temperature Monitoring of Battery Cells,” 2017.

[95] B. G. Carkhuff, P. A. Demirev, and R. Srinivasan, “Impedance-Based Battery Management System for Safety Monitoring of Lithium-Ion Batteries,” *IEEE Trans. Ind. Electron.*, vol. 65, no. 8, pp. 6497–6504, 2018.

[96] W. Haifeng, Dai;Bo, Jiang; Xuezhe, “Impedance Characterization and Modeling of Lithium-Ion Batteries Considering the Internal,” *Energies*, 2018.

[97] R. S. G. Tuttle, “Expanding the Operational Limits of theSingle-Point Impedance Diagnostic for Internal Temperature Monitoring of Lithium-ion Batteries,” *Electrochim. Acta*, vol. 174, pp. 488–493, 2015.

[98] H. P. G. J. Beelen, L. H. J. Raijmakers, M. C. F. Donkers, P. H. L. Notten, and H. J. Bergveld, “An Improved Impedance-Based Temperature Method Temperature Estimation for Li-ion Batteries,” *IFAC-PapersOnLine*, vol. 48, no. 15, pp. 383–388, 2015.

[99] J. G. Zhu, Z. C. Sun, X. Z. Wei, and H. F. Dai, “A new lithium-ion battery internal temperature on-line estimate method based on electrochemical impedance spectroscopy measurement,” *J. Power Sources*, vol. 274, pp. 990–1004, 2015.

[100] R. R. Richardson, P. T. Ireland, and D. A. Howey, “Battery internal temperature estimation by combined impedance and surface temperature measurement,” *J. Power Sources*, vol. 265, pp. 254–261, 2014.

[101] H. Beelen and M. C. F. Donkers, “Towards impedance-based temperature estimation for Li-ion battery packs,” no. November 2019, pp. 2889–2908, 2020.

6 Annexes

6.1 Annex 1

6.1.1 Limitations of Li-S batteries

Insulating nature of sulfur and its intermediates

Sulfur has an electronic conductivity of about 5×10^{-30} S cm^{-1} at 25 ºC, which often leads to low electrochemical utilization and limited rate capability. For that reason, the application of porous carbon with high surface area on the positive electrode is introduced to achieve a battery with high specific energy with a reasonable life cycle [46]. Its various intermediate products (Li_2S_x, with $8 \leq x \leq 3$) show also poor ionic and electronic conductivities, which increases the internal resistance of the battery and declines the lifecycle.[47][48] The precipitation of electrically insulating and insoluble LiPS on composite sulfur cathodes decreases the amount of active material as cycling proceeds. Hence, upon cycling Li-S cells, the sulfur becomes progressively electrochemically inactive.[5]

Slow kinetics

For an ideal electrochemical process in Li-S batteries, the lithium ions are generated after the oxidation of the lithium metal (anode) and travel across the electrolyte to the sulfur cathode during the process of discharge. The LiPS are formed when solid sulfur receives the ions and electrons during the reduction reaction, which then will change back to sulfur and lithium ions in the charging process. [4]

The drawback is that this reversible redox reaction kinetic is very slow and sluggish. The LiPS that were not converted back to sulfur and lithium ions remain in the cathode, resulting in lower discharge plateaus and higher overpotential, adding more impedance to electron and ion conduction. The reduction of the useful sulfur species leads to loss of effective capacity and energy density after some cycles.[7]

Shuttle effect LiPS: dissolution and diffusion

As referred to previously, LiPS are intermediate products formed from the structural and compositional transition of the sulfur redox reaction, and they possess high solubility in most common liquid electrolytes.[49] Polysulfides work as an activator for deposited sulfur in facilitating the redox kinetics and as a helper in mediating uniform dispersion of active materials in the cathode to access the ions and electrons.

Unfortunately, their movement within the cathode can go far beyond. The good mobility of LiPS allows them to irreversibly dissolute into the electrolyte and diffuse to the anode because of the concentration

gradient, gradually being reduced to insoluble lithium sulfides and leading to the loss of active materials. The highly dissolved polysulfides can further undergo reoxidizing back to elemental sulfur at the cathode side upon charging. This cyclic free migration phenomenon across the electrolyte between cathode and anode is called the “shuttle effect”. The loss of active materials on both the anode and cathode from the shuttle effect is the main cause of capacity degradation in Li-S batteries. During charging, some relocated lithium sulfides may shuttle back to the cathode and generate uneven re-deposition in cathode areas, which consequently result in fast degradation of capacity, low coulombic efficiency, and poor electrochemical efficiency.[50][51]

Large volume expansion

The performance of Li-S cells is often limited by the deterioration of microstructure or architecture of the electrodes associated with the volume expansion (up to 80%) and by morphology change of the active electrode material during cycling. This expansion is larger when compared to the volume expansion in Li-ion batteries. Avoiding the agglomeration of sulfur particles during cycling is difficult regardless of the initial morphology of the electrodes.[52]

Unstable lithium anode

In Li-S batteries, soluble polysulfide species in electrolytes can easily access to and react with metallic lithium with high surface area, which causes the serious corrosion of the anode and depletion of electrolyte, leading to the formation of a multiphase solid electrolyte interphase (SEI) layer composed of reaction products. The non-uniform surface cannot be sustained due to the continuous oxidation of mossy lithium and exposure to sulfur-containing species, thus, a dense passivation layer is formed, resulting in a sharp increase in polarization. All these results, along with parasitic side reactions and large lithium expansion, directly raise internal short circuit concerns, and hinder the cycle stability and charge transfer efficiency of the battery. [53]

Limited practical energy density

As previously referred, Li-S batteries have a theoretical gravimetric density of 2600 Wh Kg^{-1}, but the practical energy density is limited by important parameters such as sulfur loading, the sulfur content, the ratio of electrolyte/sulfur, and the quantity of lithium. Simultaneous integration of key cell parameters such as a reasonably sulfur content, electrolyte-starved condition, and a limited amount of lithium anode is greatly required for Li-S batteries to produce and achieve higher electrochemical performance, thus being competitive with commercial Li-ion batteries. [49] [54]

Self-discharge

Self-discharge behavior is known as the self-losing capacity process in a battery which is often an overlooked issue during resting, due to rapid and continuous LiPS redox shuttling in Li-S batteries. Self-discharge occurrence unavoidably results in the decrease of open-circuit voltage, the loss of upper discharge plateau, and discharge capacity. The self-discharge of Li-S batteries may eventually result in limited lifespan, rapid capacity degeneration, and even premature failure of sealed batteries which is considered one of the main obstacles for industrial production.[55]

6.1.2 Polymer electrolytes

Table 7 - Characteristics of polymer hosts used in electrolytes. Adapted from [8]

Polymer Host	Glass Transition Temperature [ºC]	Melting Point [ºC]	Decomposition Temperature [ºC]	Dielectric constant
PEO	-64	65	390	5.0
PAN	125	317	300	3.1
PVdF	-35	177	440 to 480	7.5 to 13.2
PMMA	105	160	360 to 390	3.0

Poly(ethylene oxide) - PEO

Polyethylene glycol is a compound derived from petroleum, and depending on its molecular weight, it can be designated poly(ethylene) oxide (Figure 3) or polyoxyethylene. PEO-based electrolytes have been widely studied for use in lithium-sulfur batteries due to having good interfacial compatibility with the electrodes and attractive electrochemical stability.[56] Li et al.[57] fabricated a PEO-gel polymer electrolyte for use in Li-S batteries aiming to improve the cycling performance. The battery exhibited a 72% capacity retention after 100 cycles at 835 $mA.g^{-1}$, which is a higher value than with a liquid electrolyte. Jeong et al.[58] studied the electrochemical properties of lithium-sulfur cells using PEO polymer electrolytes prepared in three different ways, where the effects of LiS_x and lithium sulfide on the cell cycle characteristics were investigated. Li et al.[59] prepared a gel polymer electrolyte containing PEO as a host polymer. The ionic conductivity obtained was $3.3x10^{-3}$ $S.cm^{-1}$ at room temperature, which is an excellent value.

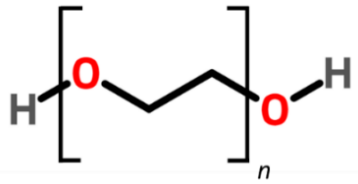

Figure 33 - Chemical structure of PEO monomer.

PEO-based electrolytes have the disadvantage of having a similar behavior to liquid electrolytes in the issue of polysulfide shuttling. Another one of the downsides of PEO is the low ionic conductivity at ambient temperature due to its tendency to crystalize at a lower temperature. [60] Although the addition of fillers, such as SiO_2, TiO_2, Al_2O_3, and ZrO_2 adsorbs polysulfides to some extent and thus improves the cycling performance of solid-state Li–S batteries [14][61][62]. Hassoun et al. [63] reported an all-solid-state lithium/sulfur cells composed of a Li_2S/C cathode, lithium metal anode, and a nanocomposite polymer as an electrolyte that delivered a discharge capacity of 300 mA.h g^{-1} at 70°C. The electrolyte was made by PEO-$LiCF_3SO_3$ with a ZrO_2 filler that increased the ionic conductivity of the composite polymeric membrane.

Polyacrylonitrile - PAN

PAN is recognized as having excellent mechanical properties and high intrinsic ionic conductivity at ambient temperature due to the higher Li^+ migration number and electrochemical stability window of the polymer. But the functional group nitrile present in this polymer (Figure 4) reacts with the lithium anode, forming a passivation layer between the anode and electrolyte, deteriorating the overall electrochemical performance and making it difficult to apply to lithium-sulfur batteries on a large scale.[64]

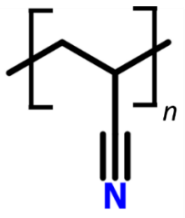

Figure 34 - Chemical structure of PAN monomer.

Again, the addition of fillers can potentially improve the performance of batteries that use this polymer host in the electrolyte. Jia et al. [65] used graphene oxide as a filler to improve the performance of a PAN-based gel electrolyte. With the addition of 1.0 wt% of graphene oxide, the polymer electrolyte presented an ionic conductivity of 2.610^{-4} S-cm^{-1} at room temperature. They also concluded that functional groups containing oxygen in graphene oxide could effectively reduce the polarity of CN-groups since the interaction between Lewis-acid type OH-groups and lone pair electrons of CN-groups softened polymer chains.

Polyvinylidene fluoride – PVdF

With a high dielectric constant, which contributes to the strong dissolution of lithium salts, PVdF is one of the most studied polymer hosts. Fluorine's shielding effects on all neighboring CH_2 groups (Figure 5) provides PVdF with good chemical resistance and thermal stability.[66] One of the major drawbacks is the interfacial instability with lithium anode that results in a weak performance for Li-S batteries.[49]

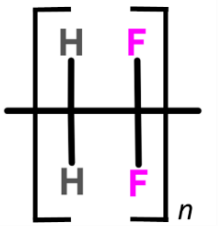

Figure 35 - Chemical structure of PVdF monomer.

Gao et al. [67] prepared a PVdF-based gel polymer electrolyte with a compact morphology to block polysulfide penetration, using a simple solution-casting method and also incorporating PEO and nano zirconium dioxide to guarantee electrolyte uptake and lithium ions mobility. The Li-S battery assembled with this electrolyte exhibited a high initial capacity of 1429 mA h g^{-1}, coulombic efficiency of 96% at 0.2 C, and improved rate performance.

Poly methyl(methacrylate) – PMMA

Discovered in the early 1930s by Rowland Hill and John Crawford, PMMA is one of the amorphous polymers that belongs to the acrylate family. It is a transparent amorphous polymer with good mechanical properties. The existence of the adjacent methyl group (CH_3) in the polymer structure is what prevents it from packing closely in a crystalline form, and from rotating freely around the C-C bonds (Figure 36). Applications of this polymer include conductive devices, polymer electrolytes, and biomedical devices. [68] [69]

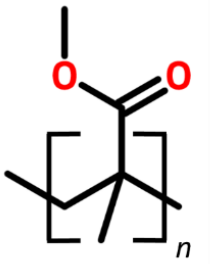

Figure 36 - Chemical structure of PMMA monomer.

A PMMA-based electrolyte is very commonly studied due to its amorphous nature and the presence of an electron-donating bulky ester functional group [O=C], which is highly active in coordinating with cations of alkali metal salts and thus easily dissociate the alkali salts. Studies also show that electrolytes based on PMMA have beneficial effects on the stabilization of the interface between the electrolyte and the lithium. But on the downside, they are brittle and have low ionic conductivity at room temperature, however, this could be improved with the incorporation of nanoparticles. [70]

Sun et al.[38] studied the effect of alumina nanoparticles on a PMMA-based electrolyte, and achieved an ionic conductivity of 1.52×10^{-4} $S.cm^{-1}$ using nanoparticles of 50 nm in diameter. Yang et al. prepared a sandwiched (PVdF/PMMA/PVdF) gel polymer electrolyte for rechargeable Li-S batteries. The PVdF layers could absorb ether-based electrolytes and then enhance lithium-ion transfer. Also, the PMMA layer was used to trap the dissolved polysulfides. The batteries with the sandwiched electrolyte showed an initial discharge capacity of 1711.8 mAh g^{-1} and the capacity retention at 1145.3 mAh g^{-1} after 50 cycles at 200 mA g^{-1}.

In general, various lithium salts such as $LiClO_4$ and $LiCF_3SO_3$ are doped to introduce the charge carriers in the polymer matrix. Between these two, $LiClO_4$ is preferred because it is relatively stable at ambient moisture and less hygroscopic than the $LiCF_3SO_3$.[71][72]

6.1.3 Review of the state-of-the-art temperature monitoring for batteries

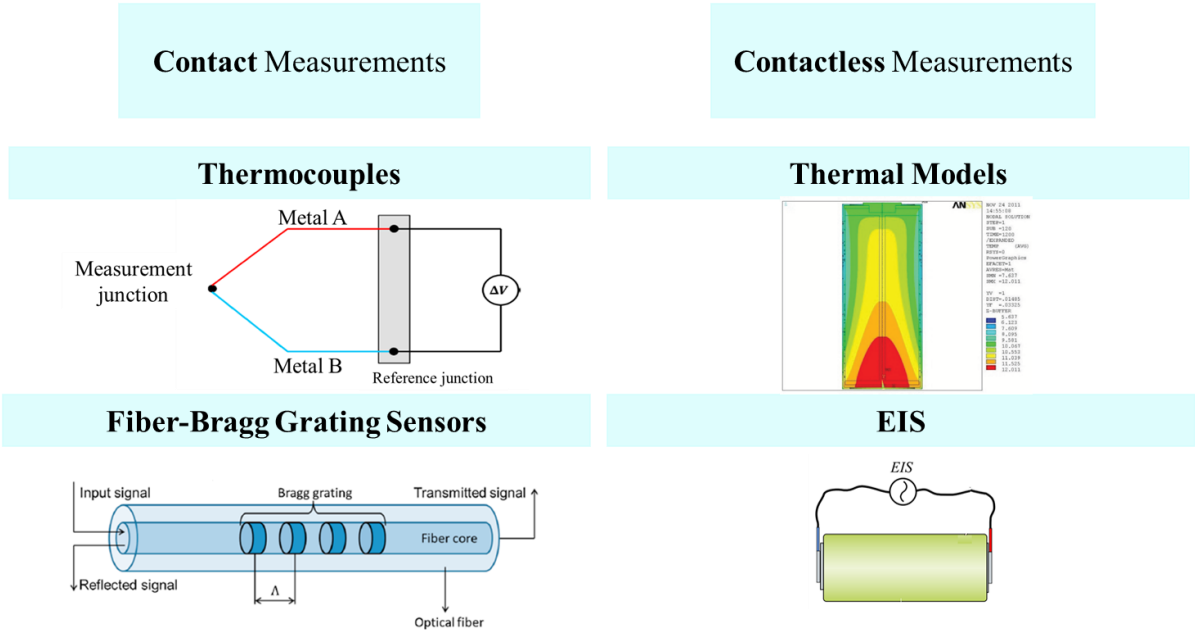

Figure 37 - Overview of the devices and methods used to monitor the temperature in batteries, Adapted from [73][74]

Thermal models

The conventional approach to temperature estimation is to use numerical electrical-thermal models conjugated with online measurements of the cell surface temperature and/or the temperature of the heat transfer medium. Using this method in combination with an algorithm such as the Kalman filtering, the cell's internal temperature can be estimated with high accuracy. [75][31]

Many kinds of thermal models have been introduced for Li-ion batteries in the past decade. In general, the models can be classified dimension-wise as one-dimensional, two-dimensional, and three-dimensional models. One-dimensional models assume simplified cell design and mode of operation with isothermal rates, constant current, lumped thermophysical properties, and constant heat generation rates. [76][77]. The two-dimensional model is better than the one-dimensional model, as it can display a basic temperature distribution. The process of overheating in Li-ion batteries is quite complicated, which combines the electrochemical process, chemical reactions, heat generation, and heat transfer. This makes the two-dimensional model not accurate enough to simulate the real case of the battery thermal runaway.[78] The more powerful and flexible in simulating the thermal performance of batteries is the three-dimensional model, the one that is normally used in assisting the design of thermal management systems.[79] In battery applications, several cells are packed together in various configurations (connected in parallel and/or series) to form a module. Several modules are then combined in series or parallel to provide the required voltage and capacity for a specific application. Therefore, the battery thermal models should be designed for the specified configuration.

Over the years, various battery thermal models of different accuracy and complexity levels have been proposed. Complex distributed electrochemical thermal models for both a single cell and a whole battery pack considering detailed heat generation and dissipation processes within and outside the battery were developed [80], [81], [82], [83], [84]. Kim et al. [85] proposed a computationally efficient thermal model for a cylindrical battery cell and its application for estimating core temperatures. The proposed model was used to identify thermal properties, and these properties were then used to estimate battery core temperature by applying the Kalman filter. The results showed that it was possible to accurately predict core temperature. Wang et al.[86] proposed a thermal model based on the finite element method to predict both surface and core temperature,

and the results showed that the errors between simulated and measured values were around 10% at different ambient temperatures and discharge rates. Figure 38 shows the simulation obtained for the core temperature distribution.

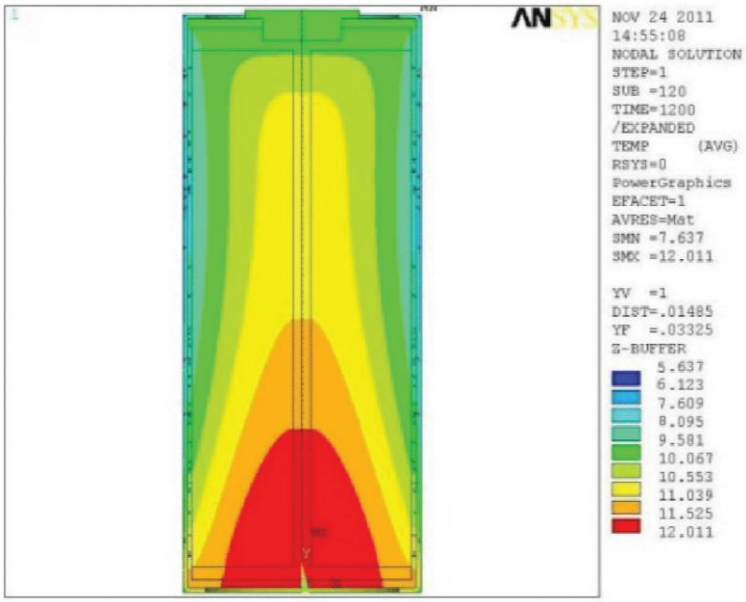

Figure 38 – Example of thermal model simulation results for internal temperature distribution at $T_0 = -10\,°C$, 3C discharge. Adapted from [86]

These electrochemical thermal models may be somewhat accurate, yet the model complexity is extremely high, and normally, the finite-element method or the Kalman filter is needed for simulation. Also, the core temperature is determined using a theoretical model that utilizes measurements obtained on the outside surface of the cell. [87]

Additionally, many battery chemical and physical parameters involved in these models are difficult to acquire. These thermal-electrical models rely on knowledge of the cell properties, heat generation rates, and thermal boundary conditions, which can be difficult to measure in practice. The internal resistance is difficult to estimate since it is a function of temperature, state of charge (SoC), and state of health (SoH). The difficulty also arises from the measurement of the thermal properties of the cell, since cells consist of many different materials combined into a layered structure, and there are unknown thermal contact resistances between the layers. [88]

Thermocouples

A thermocouple, as shown in figure 10 is an electrical device consisting of two dissimilar electrical conductors forming an electrical junction and works based on the Seebeck effect. It produces a temperature-dependent voltage as a result of the thermoelectric effect, and this voltage can be interpreted to measure temperature.

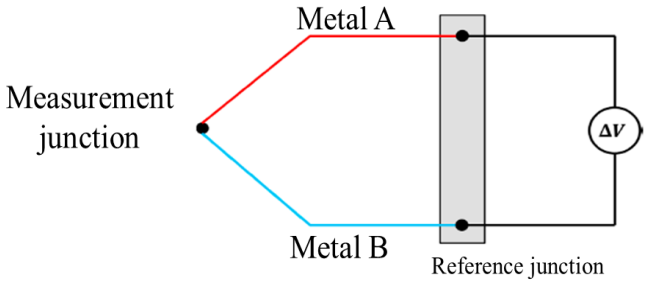

Figure 39 – Scheme of a thermocouple.[24]

They are a widely used type of temperature sensor for surface measurements, but, for example, Martiny et al.[89] developed a thin-film thermocouple for in-situ temperature measurements in a Li-ion pouch cell. They used copper and nickel as the thermocouple metals and coated the sensor with parylene, and the sensor didn't influence negatively the cell performance. Also, Mutyala et al.[90], conducted a study to monitor the temperature inside pouch cells, with flexible thin-film thermocouples (TFTC), shown in figure 11.

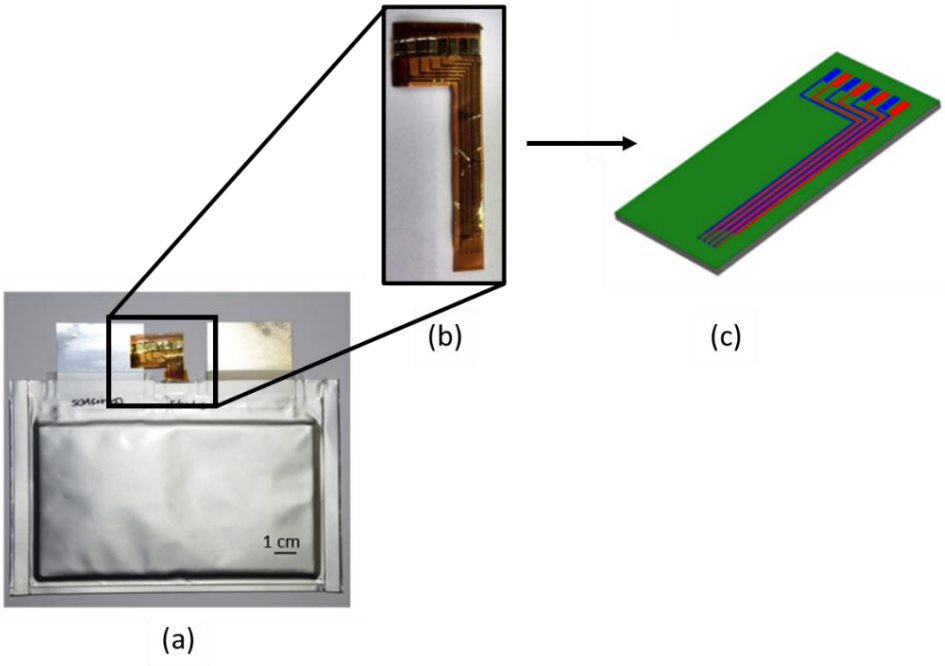

Figure 40- (a) Pouch cell with embedded flexible TFTC sensor (b) TFTC sensor (c) design of the TFTC sensor. Adapted from [90]

The sensors were fabricated, and their calibration was made before the assembly inside the pouch cell. One important point of this work is that the assembly process was minimally intrusive and semi-automated.

Thermocouples have become widely used because of the low cost, robustness, size, and temperature range (between -270 ºC to 1820 ºC). There are some drawbacks, with one of them being the sensitivity to corrosion. The sensitivity to corrosion is caused by the dissimilar metal junction. For this reason, thermocouples may need protection and maintenance. These properties make them somewhat unsuitable for long-term battery temperature measurements. Also, another important point is the nonlinearity of the electromotive force with temperature change, making it more difficult to obtain accurate temperature readings.

Fiber Bragg grating sensors

The Fiber Bragg grating (FTG) sensor is a periodic microstructure that acts as a selective wavelength mirror, and its structure is represented in Figure 41. When light from a broadband source is injected into the optical fiber, only light within a very narrow spectral region, centered on the Bragg wavelength, will be reflected, while the remaining part of the spectrum is transmitted nearly unaffected. [29]

The FGB sensor is a symmetrical structure and, as such, will always reflect the same Bragg wavelength, regardless of the direction of light. The wavelength of the reflected signal, which is called the Bragg wavelength (λ_B) has been defined as:

$$\lambda_B = 2n_{eff}\Lambda$$ Equation **(7)**

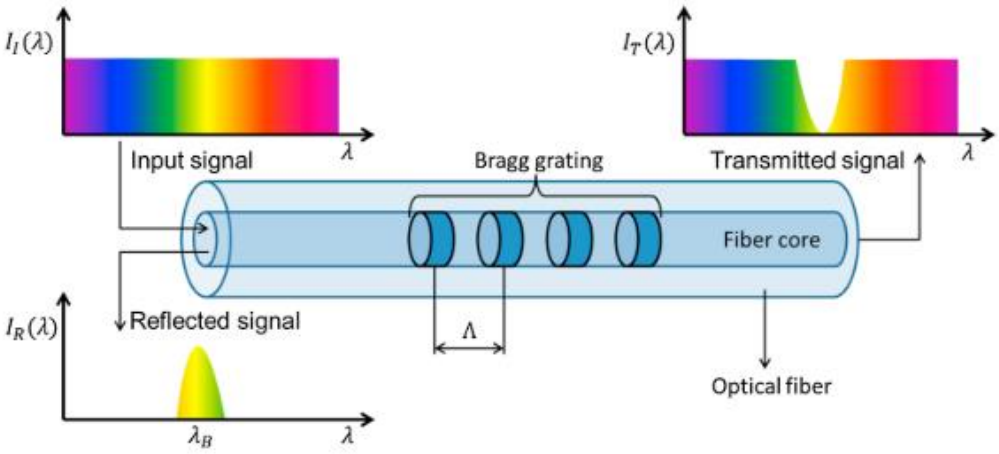

Figure 41 - Working principle of a fiber Bragg-grating sensor. [24]

Where n_{eff} is the effective core refractive index and Λ is the period of index modulation or grating spacing. A change in n_{eff} and/or Λ results in a shift in the reflected Bragg wavelength. The measurement of this wavelength shift, as a result of external influences, is the basis for FBG sensors. When a fiber is compressed or stretched, the grating spacing changes, which leads to a shift in the Bragg wavelength. This shift in Bragg wavelength can also be observed for temperature changes. This can be mainly attributed to a temperature-dependent refraction index. The influence of thermal expansion is very small and, thus, grating spacing may be neglected, the index changes are by far the most dominant effect. [91][92]

FBG sensors are becoming increasingly popular due to advantages such as small size, lightweight, passive nature, immunity to electromagnetic and radio-frequency interference, high sensitivity, and long-term reliability. Another advantage is that FBG sensors can be multiplexed, which implies that multiple FBG can be inscribed into a single optical fiber. This makes it possible to perform measurements at different locations along the fiber length. Besides, the Bragg wavelength favorably shifts linearly with temperature. Their main disadvantages are their high cost and unfamiliarity to the end-user. [93]

Sensors based on fiber Bragg gratings are an effective method to perform both static and dynamic measurements of temperature, pressure, refractive index, strain, and bending. They have also been used to monitor the strain evolution of electrodes in lithium-ion batteries. In the study by Novais et al.[32], an FBG sensor is used in monitoring a lithium-ion cell's internal and external temperature. The analysis of the internal temperature evolution during galvanostatic cycling at different C-rates provides a step forward in the understanding and safety improvement of future lithium-ion battery systems. Fortier et al. evaluated the integration of an FBG sensor inside a Li-ion battery. Results showed a difference of 10ºC between the outside and the inside temperature. [94]

Impedance-Based temperature measurements

This approach to temperature estimation uses an electrochemical impedance spectroscopy (EIS) measurement to directly collect the internal cell temperature, without using a thermal model. EIS is a non-destructive technique for characterizing the behavior of electrochemical systems. The impedance of a battery can be obtained by voltage or current excitations and, simultaneously, measuring the response. [95][96]

EIS is frequently used for extracting kinetic and transport properties of electrode materials, aging studies, modeling purposes, and determination of SoC and SoH. However, EIS can also be used to measure the internal battery temperature by relating impedance parameters, such as the phase shift, real part, or imaginary part to the temperature. In that case, this method is referred to as impedance-based temperature

indication or sensorless temperature indication. In the past years, investigations on this subject gained substantial interest since impedance-based temperature indication offers quite some advantages concerning conventional temperature measurements. [28] For instance, no external or internal hardware temperature sensors are required, thermal measurement delay is short and it measures an average/integral temperature of the active material.[97][98]

This method, which is performed at different frequency ranges using the potentiostatic mode with a small amplitude signal, is one of the most accurate methods to estimate the SoC and the SoH of the battery. [99] Temperature estimation methods based on EIS can be divided into two phases, choosing the excitation frequency (experiment design) and estimating the temperature based on the impedance measured (parameter estimation). Beelen et al.[98] presented an approach in which experiment design and parameter estimation were combined, and an improved and more accurate estimation method was deduced.

Advances have been made towards identifying the optimal impedance metric for temperature inference and extending the range of temperatures at which it can be applied. Richardson et al.[74] proposed two novel “hybrid methods”, that combine the impedance temperature detection with (i) an additional surface temperature method and (ii) a thermal model. Both methods were shown to be more accurate than the standard impedance temperature detection methods. [100]

Most of the research on using electrochemical impedance spectroscopy for temperature estimation demonstrates this functionality on the single-cell level, frequently under laboratory conditions. [101] This method has some challenges, such as the SoC and aging dependence of the impedance and the sensitivity for interference, such as (dis)charge currents and crosstalk signals. These dependencies and interference can considerably influence EIS-based temperature indications. [99]

6.2 Annex 2 – Supporting information for the procedure

6.2.1 Deposition Parameters for the sensor

Table 8 - Deposition parameters for both titanium and copper.

Deposition Parameters	Titanium	Copper
Density (g cm^{-3})	4.5	8.93
Z Factor	14.1	20.20
Thickness (nm)	20	200
Growth Rate (nm s^{-1})	0.14	0.6
Current (mA)	0.06	0.04

6.2.2 Electrolyte Formulation

For the electrolyte synthesis, the following reagents were used as received, without further purification: PMMA from Diakon, EC from Fluka with 99% purity, $LiCF_3SO_3$ from Sigma-Aldrich, and THF from Sigma-Aldrich. The production method followed was described elsewhere by Sun et al. [38]. A mixture of 0.9188g of PMMA, 0.3056g of EC, and 0.4083g of lithium salt is weighted and put on a glass recipient. The mixture is dissolved in 8 mL of THF and stirred continuously (600 rpm) at room temperature until a homogenous and transparent solution is obtained. The solution is then poured into the top of the sensor that lays on aluminum foil and left for 24 hours to allow the excess solvent to evaporate off slowly, at room temperature until thin films are formed. The produced film was also trimmed into samples for characterization of Simultaneous Thermal analysis (STA).

6.3 Annex 3 – Resistance of the sensor

Table 9 – Resistance measurements of the sensors. (With multimeter)

Sample	Resistance [Ω]	Frequency Peak 2 [GHz]	Amplitude Peak 2 [dB]
Sensor 1	25.4	1.141	-14.77
Sensor 2	26.2	1.138	-14.81
Sensor 3	28.7	1.182	-15.5
Sensor 4	32.7	1.172	-19.11
Sensor 5	28.1	1.151	-8.19
Sensor 6	22.3	1.177	-15.47
Sensor 7	27.3	1.183	-15.68
Sensor 8	30.2	1.121	-8.62
Sensor 9	23.1	1.182	-14.02
Sensor 10	21.9	1.189	-14.01
Sensor 11	24.6	1.142	-15.01
Sensor 12	30.7	1.141	-15.03
Sensor 13	29.4	1.141	-14.82

6.4 Annex 4 - Profilometer

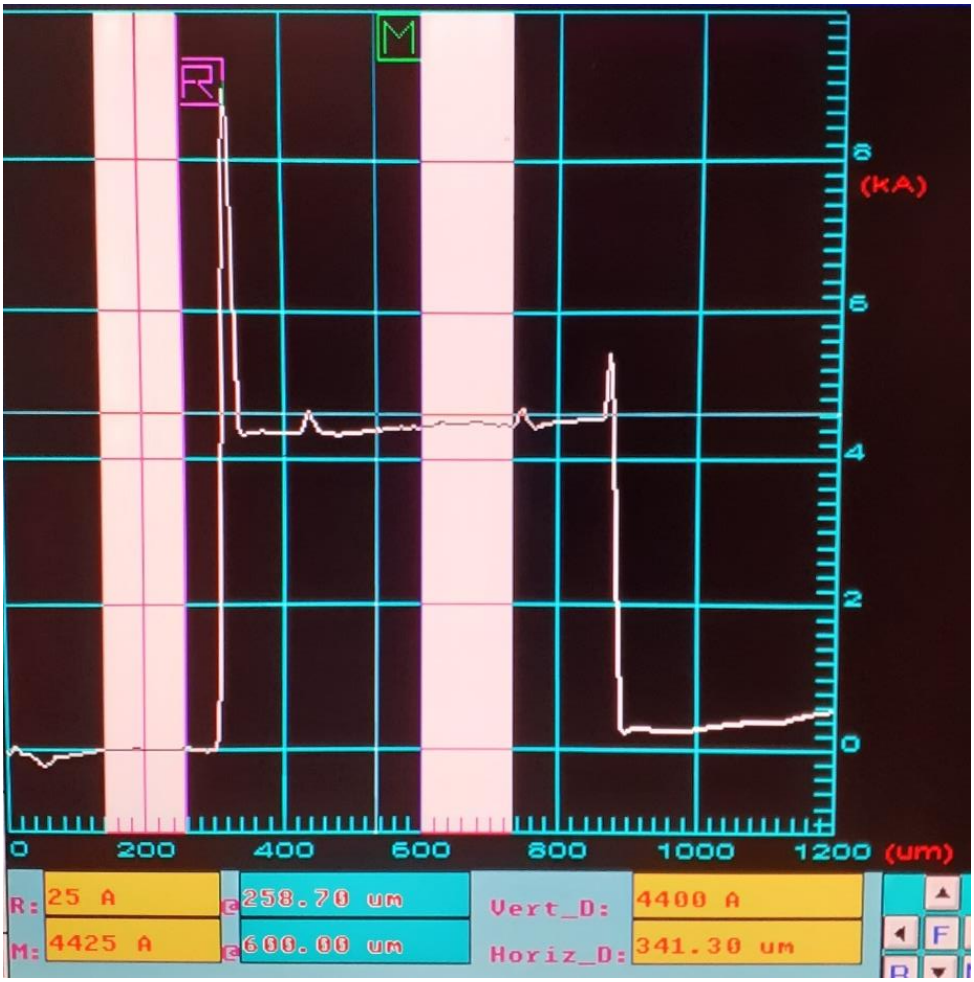

Figure 42 - Thickness of the sensor obtained by the profilometer.

6.5 Annex 5 - Simultaneous Thermal analysis (STA)

To better understand how the electrolyte behaves with the increase of temperature and to maybe help to explain some of the results obtained earlier, differential thermal analysis was performed through both thermogravimetric analyses (TGA) and simultaneously differential scanning calorimetry (DSC) measurements. These measurements are important to investigate if there is any change or degradation of the electrolyte by subjecting it to temperature variations up to 150ºC.

The TGA curve for the electrolyte is presented in figure 44. When a material is subjected to thermogravimetric analysis, it is decomposed by heat, and the bonds within molecules are broken. This technique can be useful when assessing the thermal stability of materials. The objective was to assess the thermal stability of the electrolyte.

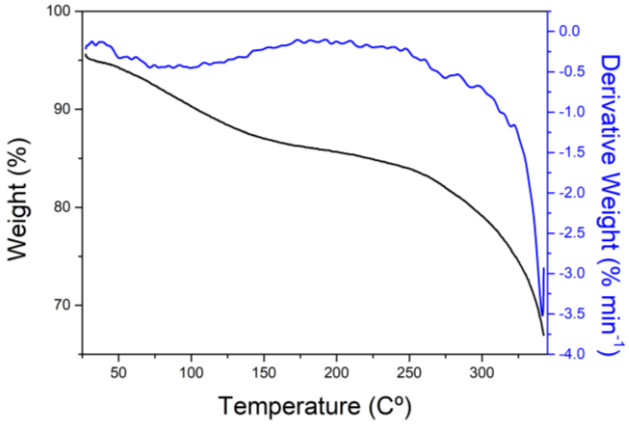

Figure 43 – TGA graphs of the electrolyte (the sample weighed 9.1g).

The TGA graph shows that the electrolyte is losing weight with the increased temperature. This continuous loss of weight can be one of the phenomena that influence the performance of the sensor.

In figure 45, where the DSC thermogram is presented, the obvious loss of weight in the electrolyte is accompanied by an endothermic peak that starts at about 315 °C in the DSC thermogram. DSC/TGA studies show that the electrolyte does not have much thermal stability after 200 ºC.

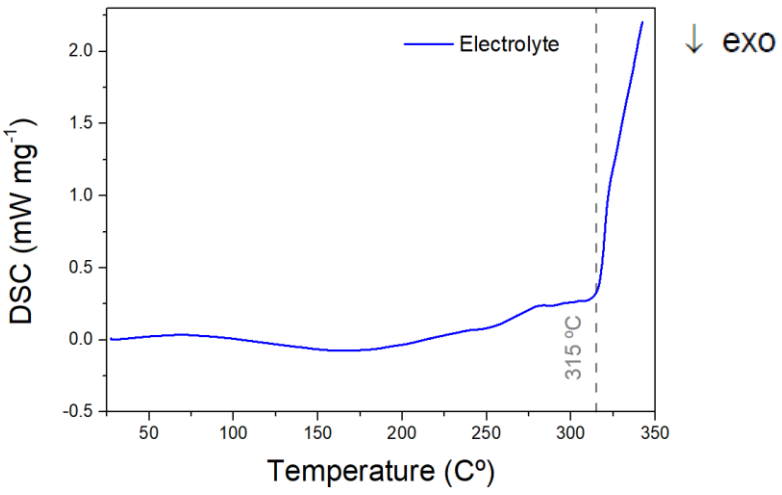

Figure 44 - DSC graph for the electrolyte.

NOVA SCHOOL OF SCIENCE & TECHNOLOGY

TEMPERATURE MONITORING FOR LITHIUM-SULFUR BATTERIES

MARGARIDA MATIAS NETO DA SILVA RIBEIRO

2021